



HAL
open science

Measuring the noise of imaging sensors in the presence of vibrations and illumination flickering: modeling, algorithm, and experiments

Frédéric Sur, Michel Grediac

► To cite this version:

Frédéric Sur, Michel Grediac. Measuring the noise of imaging sensors in the presence of vibrations and illumination flickering: modeling, algorithm, and experiments. [Research Report] RR-8672, Inria Nancy - Grand Est (Villers-lès-Nancy, France); Université Blaise Pascal; INRIA. 2015. hal-01104124

HAL Id: hal-01104124

<https://inria.hal.science/hal-01104124>

Submitted on 16 Jan 2015

HAL is a multi-disciplinary open access archive for the deposit and dissemination of scientific research documents, whether they are published or not. The documents may come from teaching and research institutions in France or abroad, or from public or private research centers.

L'archive ouverte pluridisciplinaire **HAL**, est destinée au dépôt et à la diffusion de documents scientifiques de niveau recherche, publiés ou non, émanant des établissements d'enseignement et de recherche français ou étrangers, des laboratoires publics ou privés.



Measuring the noise of imaging sensors in the presence of vibrations and illumination flickering: modeling, algorithm, and experiments

Frédéric SUR, Michel GRÉDIAC

**RESEARCH
REPORT**

N° 8672

January 2015

Project-Team Magrit & Institut
Pascal (Clermont Université)



Measuring the noise of imaging sensors in the presence of vibrations and illumination flickering: modeling, algorithm, and experiments

Frédéric SUR*, Michel GRÉDIAC†

Project-Team Magrit & Institut Pascal (Clermont Université)

Research Report n° 8672 — January 2015 — 52 pages

Abstract: This report discusses camera noise estimation from a series of raw images of an arbitrary natural static scene, acquired with the same camera settings. Although it seems natural to characterize noise from the random time fluctuation of pixel intensity, it turns out that these fluctuations may also be caused by illumination flickering and mechanical micro-vibrations affecting the camera. In this context, the contributions are twofold. First, a theoretical model of image formation in the presence of illumination flickering and of vibrations is discussed. This parametric model is based on a Cox process. It is shown that illumination flickering changes the standard affine relation between noise variance and average intensity to a quadratic relation. Second, under these conditions an algorithm is proposed to estimate the main parameters governing sensor noise, namely the gain, the offset, and the read-out noise. The rolling shutter effect, which potentially affects the output of any focal-plane shutter camera, is also considered. Experiments show that this simple method gives results consistent with the photon transfer method which needs a special experimental setting and several data acquisitions, and with an algorithm based on a single image. The main practical result is to show that flickering, which is generally considered as an artifact, plays here a positive role since it finally enables us to estimate any of the sensor parameters. This report provides additional experiments to a published paper.

Key-words: Sensor noise measurement, Poisson-Gaussian noise model, illumination flickering, Cox process, rolling shutter effect.

* LORIA UMR 7503 - projet Magrit, Université de Lorraine, CNRS, INRIA, Campus Scientifique BP 239, 54506 Vandœuvre-lès-Nancy cedex, France.

† Institut Pascal UMR CNRS 6602, Université Blaise Pascal BP 10448, 63000 Clermont-Ferrand, France

**RESEARCH CENTRE
NANCY – GRAND EST**

615 rue du Jardin Botanique
CS20101
54603 Villers-lès-Nancy Cedex

Mesure du bruit des capteurs d'images en présence de vibrations et d'un scintillement de l'illumination: modélisation, algorithme et expériences

Résumé : ce rapport traite de l'estimation du bruit d'une caméra à partir d'une séquence d'images brutes d'une scène naturelle statique, acquise avec des réglages de caméra constants. Bien qu'il semble naturel de caractériser le bruit à partir des fluctuations aléatoires de l'intensité des pixels au cours du temps, il s'avère que ces fluctuations peuvent être causées par le scintillement de l'illumination et par des micro-vibrations mécaniques affectant la caméra. Dans ce cadre, nous proposons deux contributions. Un modèle théorique de la formation d'une image en présence de scintillement et de vibrations est d'abord discuté. Ce modèle paramétrique est basé sur un processus de Cox. Il est démontré que le scintillement de l'illumination transforme la relation affine classique entre variance du bruit et intensité moyenne en une relation quadratique. Dans ses conditions, un algorithme est ensuite proposé pour estimer les principaux paramètres régissant le bruit d'un capteur, à savoir le gain, le biais, et le bruit de lecture. L'effet « rolling shutter », qui peut affecter la sortie de toute caméra à obturateur plan focal, est également considéré. Des expériences montrent que cette méthode simple donne des résultats cohérents avec la méthode du transfert de photons qui demande un protocole expérimental spécifique et plusieurs acquisitions, et avec un algorithme basé sur une image unique. Le résultat pratique principal est de montrer que le scintillement joue ici un rôle positif car il permet d'estimer tous les paramètres du bruit du capteur. Ce rapport ajoute des expériences supplémentaires à un article publié.

Mots-clés : mesure du bruit d'un capteur, modèle de bruit de Poisson-Gauss, scintillement de l'illumination, processus de Cox, effet « rolling shutter ».

Contents

1	Introduction	4
2	Sensor noise modeling in the presence of a flickering illumination and vibrations	6
2.1	Modeling raw data from a linear camera	7
2.2	Noise variance against intensity expectation	8
2.3	Discussion	10
2.3.1	Sample mean and sample variance	10
2.3.2	Non-static scenes	10
2.3.3	Link with ICCD	10
2.3.4	Spatial non-uniformity	11
3	Estimating noise parameters	11
3.1	Removing pixels affected by physical vibrations or clipping	11
3.2	Flicker reduction	12
3.3	Linear regression	15
3.4	Summary: algorithm	15
3.5	Balancing the rolling shutter effect	15
4	Experimental results	18
4.1	Running example	18
4.2	Synthetic data	20
4.3	Real data	28
4.3.1	PCO Sencam QE	28
4.3.2	Canon EOS 350D and EOS 6D cameras	34
4.3.3	Experiments with a stable light	44
5	Conclusion	48

1 Introduction

Noise is an undesired yet unavoidable feature of digital imaging sensors. Since consumer cameras are expected to offer the most pleasing-to-the-eye images, denoising algorithms have become crucial parts of the image processing chain. Recent papers such as [34] or [41] argue that an accurate modeling of the noise is important for these algorithms. Not only is it needed in denoising applications, but it is also of utmost importance for assessing the metrological performance of contactless measurement systems which spread quickly in various fields of engineering. For example in experimental mechanics, assessing the noise level in displacement and strain maps obtained with such measurement systems and establishing its link with camera sensor noise is a key issue, as illustrated by recent papers (see, e.g., [25, 27, 42, 45, 60, 61]). Although the Gaussian white noise assumption is widely spread, this rough model is inadequate when considering metrological performance assessment or state-of-the-art denoising applications. In the case of raw data from a CCD or CMOS sensor, the authors of [26] identify four major sources of noise, namely residual dark current (depending on the ambient temperature and on the exposure time), shot noise (modeling the uncertainty in the electron count at a photosite), read-out noise (due to on-chip output amplifier), and quantization noise. The raw output of a linear camera (i.e., the raw sensor output, without any image processing) is proportional to the quantity of light photons arriving at a CCD sensor cell, plus a dark current, and read-out noise. The following stochastic model (or slight variations) is often used [4, 10, 21, 24, 26], yielding a heteroscedastic signal-dependent noise,

$$u(x, y) = g \eta_{p(x,y)+d(x,y)}(x, y) + \delta(x, y) \quad (1)$$

where:

- $u(x, y)$ is the intensity or gray level measured at the photosite corresponding to the pixel (x, y) in the raw output image;
- $g > 0$ is the gain of the electronic system;
- The number of generated electrons $\eta_{p(x,y)+d(x,y)}$ at (x, y) is a random variable following a Poisson distribution of mean value $p(x, y) + d(x, y)$, assumed to be spatially independently distributed. Here $p(x, y)$ is the number of electrons produced by a part of the incident photons (the proportion depends on the quantum efficiency of the device at a given wavelength) and $d(x, y)$ is the number of “dark” electrons generated during the exposure time;
- $\delta(x, y)$ is a Gaussian white noise of mean μ (fixed offset value imposed by the sensor manufacturer) and variance σ^2 (caused by readout and quantization noise).
- The random variables $\eta_{p(x,y)+d(x,y)}(x, y)$ and $\delta(x, y)$ are independent.

In this formulation, the limited range (caused by the finite capacity of each photosite) and the quantized nature of the gray-level u are ignored.

In usual experimental setting (common temperature and exposure time equal to a fraction of a second) the dark current is negligible relative to the photo-electron count [4, 26]. In the remainder of this report, we set $d = 0$. In addition, most color camera sensors are actually equipped with a Bayer filter mosaic. In this case, (1) holds for each of the color channels.

Within the model of (1), the expectation and the variance of any Poisson variable being equal, it is possible to compute [10, 19, 21, 24, 47]

$$\begin{cases} E(u(x, y)) = gp(x, y) + \mu \\ \text{Var}(u(x, y)) = g^2p(x, y) + \sigma^2 \end{cases} \quad (2)$$

where E and Var denote respectively the expectation and the variance. The following affine relation consequently holds:

$$\text{Var}(u(x, y)) = gE(u(x, y)) + \sigma^2 - g\mu \quad (3)$$

As noted in [24], it is possible that $\sigma^2 - g\mu < 0$.

Estimating the whole set of noise parameters can be achieved by the so-called “photon transfer method” [3, 28] which needs a controlled experimental setting and several data acquisitions. Estimating the slope g and the intercept $\sigma^2 - g\mu$ in (3) is sufficient for many applications. For instance, the first task of many image denoising algorithms is to stabilize the variance using, e.g., the generalized Anscombe transform [39, 43] (after [5]) which only needs these two parameters. Another application to camera model identification is presented in [56]. In order to estimate the slope and the intercept in (3), a simpler method than the photon-transfer method is sought. This is the goal of several papers, where these parameters are estimated by using a single image. The sample mean and variance can be evaluated on homogeneous image regions [19, 24, 47], or a selection of small homogeneous patches [10, 36], which is likely to fail with a cluttered scene giving highly textured images. In this case, the authors of [57] model image textures as 2D fractional Brownian motions and propose an estimator of the signal-dependent noise affecting such textures. The approach of [24] has also been made more robust to high-frequency textures in [6]. A joint estimation of the noise parameters and of an implicit segmentation is proposed in [31]. The authors of [7] eliminate the selection of homogeneous patches by modeling arbitrary patches as Gaussian mixtures. While the above-mentioned papers are mainly based on parametric regressions of variance against expectation plots, a recent approach consists in estimating sensor parameters so that a variance stabilization function performs at best, as in [32] under the Poisson or [40, 46] under the Poisson-Gaussian assumptions. Non-parametric approaches based on the estimation of a noise level function of arbitrary shape are also available (see, e.g., [35] and more recently [14]). These latter approaches are not within the scope of this report, which is focused on parametric estimation.

Instead of using spatial statistics of a single image, it is also possible to use temporal statistics of a series of images. An image stacking approach would simply consist in taking a series of images of a static scene at different times with the same camera settings, and in computing afterward the sample mean and variance at a given pixel, as in [23]. It turns out, however, that the random fluctuations of the stacked pixel intensities are not solely the result of the digital noise modeled by (1), as illustrated in Figure 1. First, even if the camera is fixed to a heavy tripod, mechanical micro-vibrations are likely to affect the sensor, hence the imaged scene. It is well known that concrete floor slabs on which camera or imaged objects rest are prone to vibrations [20]. This phenomenon is very difficult to avoid without a costly dedicated setting such as a vibration insulated optical table, or an optical image stabilization system. For example, it has been demonstrated in [59] that the pixel intensity fluctuations along edges of digitized aerial images are temporally correlated because of vibrations during the scanning process. The movement of the mirror or of the shutter in a single-lens reflex (SLR) camera, or the cooling device in a high-end camera may also cause vibrations. The atmospheric turbulence is another potential source of instability of the imaged scene. Even if these perturbations yield motions with a tiny amplitude, they are all the more noticeable as the photosite density is high or the focal length is long. Another important external source of pixel intensity fluctuations is the flickering of the illumination source. A number of reasons may cause this phenomenon, among which the domestic alternative current supplying artificial lights [13]. Certain light sources are particularly affected, such as neon tube lights [38], or poorly designed LEDs [2]. A slight variability of the exposure time caused by mechanical or electronic imperfections of the shutter would cause an equivalent effect. Interestingly, a similar deterministic phenomenon can be noticed in fluorescence imaging:

an exponential decay of the photon count caused by photobleaching is considered in [30] where the model parameters are estimated using an iterative Expectation-Minimization approach. In the context of denoising from a burst of images, the authors of [12] find out that the bursts suffer from changes in the illumination conditions, which makes it impossible to estimate the noise level from intensity changes along time. They circumvent this problem by histogram equalization [17]. Although this method proved to be effective for image denoising, such an approach does not give any guarantee in the estimated noise parameters and thus cannot be used in a metrological framework.

In the end, mechanical vibrations and illumination flickering prevent the sample mean and the sample variance estimated by time-averaging from satisfying the affine relation given by (3). The effect of the sole vibrations on noise measurement has been investigated in the case of pseudo-periodic grid images [52, 55]. This was motivated by the characterization of the metrological performances of the grid method [8, 25, 53] in experimental solid mechanics. A short discussion of the flickering effect on noise measurement is available in [51]. This research report is an extended version of [54].

Contribution and organization of the report. The contribution of this report is to investigate the effect of mechanical vibrations and light flickering on the estimation of the noise parameters using image stacking. A theoretical model is proposed in Section 2 and a practical algorithm is discussed in Section 3. The model is based on quite general assumptions. In particular, no periodicity or pseudo-periodicity assumption on the illumination variability is needed. The vibrations are assumed to be of limited amplitude (typically smaller than one pixel), and the algorithm does not need to estimate their amplitude from image to image. Contrary to [22, 24], intensity clipping is not taken into account in the model, which also overlooks defective pixels and blooming effect. Clipped data and defective pixels are simply eliminated in a preliminary step. Under a flickering illumination, the variance of the pixel intensity fluctuation is proved to be a quadratic function of the average intensity, instead of the usual affine dependence. Although the methods based on a single image are not affected by these phenomena, the present algorithm, as any stacking method, does not need any explicit segmentation step. We demonstrate that light flickering makes it possible to estimate all the sensor parameters, namely the gain, offset and read-out noise level. Although very accurate estimations of these parameters (apart from non-uniformity problems) can only be achieved by the photon transfer method, we show that stacking 100 images affected by flickering is often sufficient to get a reasonable estimation. In addition, we mention a workaround to deal with the rolling shutter effect, which especially affects cameras with a focal-plane shutter, such as SLR cameras. The estimation process is evaluated on synthetic and real data (raw images from two SLR cameras and a high-end CCD camera) in Section 4. As a sanity check, it is also compared with the photon transfer method and to the software implementing [24], which only needs a single image. We conclude with Section 5.

A Matlab code is available at the following URL:
<http://www.loria.fr/%7Esur/software/NESIF/>

2 Sensor noise modeling in the presence of a flickering illumination and vibrations

The aim of this section is to model the measured intensity at a pixel along time, under a flickering illumination and mechanical vibrations affecting the experimental setup, and to link the time variance to the expected intensity.

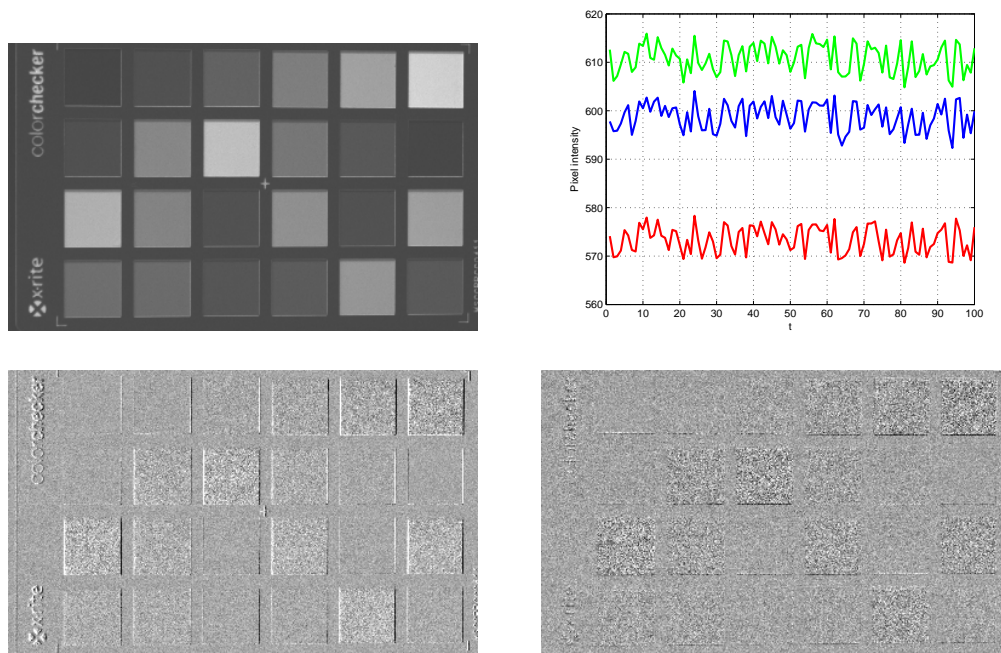


Figure 1: An X-rite Colorchecker, illuminated by a neon light, is imaged by a Canon EOS 350D camera (ISO 100) equipped with a 50mm lens and fixed to a tripod. A burst of 100 images is taken. Top left: A raw image (red channel) from the series. Top right: An average pixel intensity is computed over 100 pixels belonging to the same color patch in order to remove the random digital noise. The graph depicts the evolution of this average intensity at three distant locations belonging to different color patches. In-phase fluctuations can be seen; they are due to light flickering. Bottom: the two images correspond to two examples of a difference between two distant images of the burst (same gray value scale). In the ideal vibration-free case, the difference image would only consist in a noise proportional to the pixel intensity. Here, edges can be seen and are more or less pronounced according to the direction and the gray level difference between a patch and the black background color. They are caused by mechanical micro-vibrations.

2.1 Modeling raw data from a linear camera

A series of T images of a static scene is assumed to be available. The number of emitted photo-electrons at a given photosite being proportional to the number of incoming photons (through the quantum efficiency), the average number of photo-electrons at a photosite of the t -th image can be expressed as $(1 + \gamma_t)p(x + \alpha_t, y + \beta_t)$ where

- (α_t, β_t) is the translation vector modeling the sensor in-plane displacement due to vibrations between an unknown reference image and the t -th image;
- $1 + \gamma_t$ is the relative fluctuation of the illumination intensity.

Within the assumptions of Section 1, the intensity $u(x, y, t)$ at pixel (x, y) of the t -th image is modeled by

$$u(x, y, t) = g \eta_{(1+\gamma_t)p(x+\alpha_t, y+\beta_t)}(x, y, t) + \delta(x, y, t) \quad (4)$$

where the random variables η and δ are time-independent and spatially distributed as above. Adding constant terms to x and y means that we only consider translations, which corresponds to what is observed in practice in all the experiments described in Section 4 below.

Both processes γ_t and (α_t, β_t) are modeled as an independently and identically distributed 0-mean random process. The variance of γ is noted σ_γ^2 and the 2×2 covariance matrix of (α_t, β_t) is $\text{Cov}(\alpha, \beta)$.

In this model, the intensity of the Poisson variable is also a random process. It is called a mixed doubly stochastic Poisson process, or Cox process after [15]. The intensity $u(x, y, t)$ is thus a realization of a Cox-Gaussian process. The goal of the following section is to calculate a relation between the variance of u and its expectation.

2.2 Noise variance against intensity expectation

In the following calculations, we make use of the law of the total expectation and of the law of the total variance: if X is an integrable random variable and Y is another random variable, then $E(X) = E(E(X|Y))$ and $\text{Var}(X) = E(\text{Var}(X|Y)) + \text{Var}(E(X|Y))$. We also recall that if X and Y are two independent random variables, then $E(XY) = E(X)E(Y)$. For reasons of concision, we skip the mention to (x, y, t) after u and δ , and to (x, y) after p .

Let η_λ be a Cox process: this means that, conditional on $\lambda = l$, η_l is a Poisson process of mean value l . With the law of the total expectation and the law of the total variance, we obtain:

$$\begin{cases} E(\eta_\lambda) = E(E(\eta_\lambda|\lambda)) = E(\lambda) \\ \text{Var}(\eta_\lambda) = E(\text{Var}(\eta_\lambda|\lambda)) + \text{Var}(E(\eta_\lambda|\lambda)) = E(\lambda) + \text{Var}(\lambda) \end{cases} \quad (5)$$

This expression of the variance means that a Cox process is overdispersed relative to the Poisson process [16]. Under a flickering light and/or vibrations, the time-variance of the intensity at a given pixel thus always overvalues the expected variance given by the standard Poisson-Gaussian model. More precisely, we calculate from the properties of the expectation and variance of a Cox process:

$$E(u) = E(g\eta_{(1+\gamma_t)p(\cdot+\alpha_t, \cdot+\beta_t)} + \delta) \quad (6)$$

$$= gE((1+\gamma_t)p(\cdot+\alpha_t, \cdot+\beta_t)) + \mu \quad (7)$$

$$= gE(p(\cdot+\alpha_t, \cdot+\beta_t)) + \mu \quad (8)$$

(where \cdot denotes either x or y), since γ_t and $p(\cdot+\alpha_t, \cdot+\beta_t)$ are independent, and $E(\gamma_t) = 0$. Moreover,

$$\text{Var}(u) = \text{Var}(g\eta_{(1+\gamma_t)p(\cdot+\alpha_t, \cdot+\beta_t)} + \delta) \quad (9)$$

$$= g^2E((1+\gamma_t)p(\cdot+\alpha_t, \cdot+\beta_t)) \quad (10)$$

$$+ g^2\text{Var}((1+\gamma_t)p(\cdot+\alpha_t, \cdot+\beta_t)) + \sigma^2$$

$$= g^2E(p(\cdot+\alpha_t, \cdot+\beta_t)) + g^2(1+\sigma_\gamma^2)E(p^2(\cdot+\alpha_t, \cdot+\beta_t)) \quad (11)$$

$$- g^2(E(p(\cdot+\alpha_t, \cdot+\beta_t)))^2 + \sigma^2$$

Indeed, with the law of the total variance:

$$\text{Var}((1+\gamma_t)p(\cdot+\alpha_t, \cdot+\beta_t)) = E(\text{Var}((1+\gamma_t)p(\cdot+\alpha_t, \cdot+\beta_t)|\alpha_t, \beta_t)) \quad (12)$$

$$+ \text{Var}(E((1+\gamma_t)p(\cdot+\alpha_t, \cdot+\beta_t)|\alpha_t, \beta_t))$$

$$= \sigma_\gamma^2E(p^2(\cdot+\alpha_t, \cdot+\beta_t)) + \text{Var}(p(\cdot+\alpha_t, \cdot+\beta_t)) \quad (13)$$

$$= (1+\sigma_\gamma^2)E(p^2(\cdot+\alpha_t, \cdot+\beta_t)) \quad (14)$$

$$- (E(p(\cdot+\alpha_t, \cdot+\beta_t)))^2$$

since $\text{Var}(p(\cdot + \alpha_t, \cdot + \beta_t)) = E(p^2(\cdot + \alpha_t, \cdot + \beta_t)) - (E(p(\cdot + \alpha_t, \cdot + \beta_t)))^2$, hence (11).

As we can see from (8) and (11), the term $E(p^2(x + \alpha_t, y + \beta_t))$ prevents us from writing $\text{Var}(u)$ as a simple function of $E(u)$. Nevertheless, inspired by the Delta-method [44] we can use a second-order Taylor series expansion:

$$\begin{aligned} p(x + \alpha_t, y + \beta_t) &= p(x, y) + (\alpha_t, \beta_t) \nabla p(x, y) \\ &\quad + \frac{1}{2} (\alpha_t, \beta_t) H_p(x, y) (\alpha_t, \beta_t)^T + R_p(x, y, \alpha_t, \beta_t) \end{aligned} \quad (15)$$

with ∇ the gradient, $H_p(x, y)$ the Hessian matrix of p at (x, y) , and the remainder R_p being a multivariate polynomial in (α_t, β_t) with monomials of total degree larger than 3.

On the one hand, taking first the square of (15), then the expectation:

$$\begin{aligned} E((p^2(\cdot + \alpha_t, \cdot + \beta_t))) &= p^2 + \nabla p^T \text{Cov}(\alpha, \beta) \nabla p \\ &\quad + pE((\alpha_t, \beta_t) H_p(\alpha_t, \beta_t)^T) + M_p^1(\cdot, \cdot, \alpha_t, \beta_t) \end{aligned} \quad (16)$$

where M_p^1 is a linear combination of mixed moments of (α_t, β_t) of order larger than 3. To establish (16), we have used:

$$\begin{aligned} E(((\alpha_t, \beta_t) \nabla p)^2) &= E(\alpha_t^2 (\partial p / \partial x)^2 + E(\beta_t^2 (\partial p / \partial y)^2 \\ &\quad + 2E(\alpha_t \beta_t) (\partial p / \partial x) (\partial p / \partial y)) \end{aligned} \quad (17)$$

$$= \nabla p^T \text{Cov}(\alpha, \beta) \nabla p \quad (18)$$

On the other hand, taking first the expectation of (15) then its square:

$$\begin{aligned} (E(p(\cdot + \alpha_t, \cdot + \beta_t)))^2 &= \left(p + E\left(\frac{1}{2} (\alpha_t, \beta_t) H_p(\alpha_t, \beta_t)^T\right) \right. \\ &\quad \left. + E(R_p(\cdot, \cdot, \alpha_t, \beta_t)) \right)^2 \end{aligned} \quad (19)$$

$$= p^2 + pE((\alpha_t, \beta_t) H_p(\alpha_t, \beta_t)^T) + M_p^2(\cdot, \cdot, \alpha_t, \beta_t) \quad (20)$$

where

$$\begin{aligned} M_p^2(\cdot, \cdot, \alpha_t, \beta_t) &= \left(E\left(\frac{1}{2} (\alpha_t, \beta_t) H_p(\alpha_t, \beta_t)^T\right) + E(R_p(\cdot, \cdot, \alpha_t, \beta_t)) \right)^2 \\ &\quad + 2pE(R_p(\cdot, \cdot, \alpha_t, \beta_t)) \end{aligned} \quad (21)$$

is a combination of mixed moments of (α_t, β_t) of order larger than 3, of squares of moments of order 2, and of products of moments of order 2 and larger.

With (16) and (20), we obtain

$$\begin{aligned} E((p^2(x + \alpha_t, y + \beta_t))) &= (E(p(x + \alpha_t, y + \beta_t)))^2 + \nabla p^T \text{Cov}(\alpha, \beta) \nabla p \\ &\quad + M_p(x, y, \alpha_t, \beta_t) \end{aligned} \quad (22)$$

with $M_p = M_p^1 - M_p^2$.

By substituting in Equation (11) $gE(p(\cdot + \alpha_t, \cdot + \beta_t))$ by $E(u) - \mu$ (cf (8)) and $E((p^2(\cdot + \alpha_t, \cdot + \beta_t)))$ by the expression given by (22), we eventually obtain:

$$\begin{aligned} \text{Var}(u) &= \sigma_\gamma^2 E(u)^2 + (g - 2\mu\sigma_\gamma^2) E(u) + \sigma^2 - g\mu + \sigma_\gamma^2 \mu^2 \\ &\quad + (1 + \sigma_\gamma^2) \nabla E(u)^T \text{Cov}(\alpha, \beta) \nabla E(u) + M_p(x, y, \alpha_t, \beta_t) \end{aligned} \quad (23)$$

Under the mild assumption that the vibrations follow a Gaussian process, moments of order larger than 3 are products of moments of order 2 [29], which justifies that, for small vibrations, the term M_p is negligible compared with the term with $\text{Cov}(\alpha, \beta)$.

We have proved that, because of flickering, the affine relation of (3) between the variance and the expected pixel intensity transforms into a quadratic relation, and that the vibrations give an additional bias.

At a pixel where the gradient is negligible (or more generally where the neighboring pixels have the same intensity), the relation simply writes:

$$\text{Var}(u) = \sigma_\gamma^2 E(u)^2 + (g - 2\mu\sigma_\gamma^2)E(u) + \sigma^2 - g\mu + \sigma_\gamma^2 \mu^2 \quad (24)$$

Of course, $\sigma_\gamma = 0$ simplifies the quadratic expression (24) into the affine one given in (3). Moreover, even in the flicker-free case, (23) shows that the variance estimation is always an over-estimation of the expected variance, because of the vibrations.

2.3 Discussion

Several properties of the model are now discussed.

2.3.1 Sample mean and sample variance

In the remainder of this report, the sample mean $1/T \sum_{t=1}^T X(t)$ of any random process $(X(t))_{1 \leq t \leq T}$ is noted \bar{X} . The sample mean $\bar{u}(x, y)$ is an unbiased estimator of $gE(p(x + \alpha_t, y + \beta_t)) + \mu$. Since its variance is equal to $\sum_t \text{Var}(u(x, y, t))/T^2 = \mathcal{O}(1/T)$, this estimator is also consistent. (\mathcal{O} denotes Landau's "big-O".) The unbiased time sample variance $\bar{\sigma}_u^2(x, y)$ has an expectation equal to $\text{Var}(u(x, y, t))$ and it is well known that its variance decreases as $1/T$ as soon as the distribution kurtosis is finite. The empirical variance is thus also a consistent estimator of the variance.

Disregarding the vibrations, it should be noted that flickering makes it impossible to estimate the noise parameters g and $\sigma^2 - g\mu$ with a quadratic regression (because of the σ_γ^2 term), contrary to the existing parametric methods based on a single image cited in the introduction, where linear regression is sufficient.

2.3.2 Non-static scenes

The preceding calculation assumes that the scene is static and that the vibrations equally affect all the sensor pixels. Nevertheless, it is common for an outdoor scene to have at least some slightly moving parts. For example, the scene may show trees swinging because of the wind, or passers-by, which would affect the series of images. It should be noted that (23) holds locally, that is, the 2D random process (α_t, β_t) may depend on (x, y) . However, in the case of large movements, the Taylor expansion no more holds in (15). If the non-static part of the scene is limited, the experimental results presented here are likely to hold, but in general, non-static scenes are clearly out of the scope of this report.

2.3.3 Link with ICCD

It has been shown in [9] (cited by [48, 49]) that a quadratic relation with different parameters also holds when considering intensified charged couple device (ICCD). The difference with the standard CCD model described in (1) is that the gain g is modeled in an ICCD as a random variable. In the present model, the gain is fixed but the intensity of the Poisson process is a random variable.

2.3.4 Spatial non-uniformity

The standard model of equation (3) assumes that the gain, the quantum efficiency and the dark noise are uniform. However, manufacturing variability and component tolerances make these quantities to vary from pixel to pixel, yielding the so-called dark signal non-uniformity (DSNU) and photo response non-uniformity (PRNU) [3, 26, 28]. These departures from ideality amount in (3) (and in the following calculations) to consider γ_t , g , and δ as functions of (x, y) , in order to take into account the non-uniformity of, respectively, quantum efficiency, gain, and dark signal.

This means that the scatter plots of time sample variance against time sample mean shall show a variability not only caused by the usual variability of any sample estimator, but also caused by DSNU and PRNU. The authors of [48] observe gradual spatial non-uniformity in the case of ICCD and design a parametric model to deal with it. In CCD or CMOS, it is known that PRNU gives an additional intensity variability up to some percent [1, 3]. The effect on the quadratic relation caused by flickering is all the more important because of the quadratic term.

In the remainder of this report, we do not take PRNU and DSNU into account, as in all the papers cited in the introduction. Nevertheless, these phenomena explain a part of the variability in the expected relations.

3 Estimating noise parameters

It is in fact possible to remove the effect of light flickering in the variance estimation. The scene is indeed static, shows no moving object (apart from the micro-vibrations), and the flickering is assumed (until Section 3.5) uniform over each image, contrary to the more complicated classic flicker removal problem in movies, see, e.g., [18]. The proposed algorithm to estimate noise parameters consists of the following steps:

1. Eliminate the pixels where the gradient is too large to be caused by random noise using a statistical test, in order to keep only pixels such that (24) is satisfied. This pre-processing step permits us to eliminate the bias caused by the vibrations. Clipped or defective pixels are also eliminated. See Section 3.1.
2. Identify the flicker parameter γ_t for each image of the stack, and remove the effect of flicker in the sample variance estimated from the image stack. See Section 3.2.
3. Estimate the noise parameters using linear regression on flicker-reduced intensity variation. See Section 3.3.

As we shall see, the output of the proposed algorithm is an estimation of all parameters of the linear camera model, namely g , μ , and σ , and not only of the parameters g and $\sigma^2 - g\mu$ of the affine relation (3).

3.1 Removing pixels affected by physical vibrations or clipping

The relationship given by (23) shows that physical vibrations bias the estimation of the pixel intensity variance as a function of the gradient of the expected intensity. In order to remove the effects of the vibrations, we keep only pixels where the local gradient is likely to be due to random noise instead of an actual edge. The gradient being evaluated here with a centered difference scheme, its squared Euclidean norm is

$$\begin{aligned} \|\nabla \bar{u}(x, y)\|^2 &= (\bar{u}(x+1, y) - \bar{u}(x-1, y))^2/4 \\ &\quad + (\bar{u}(x, y+1) - \bar{u}(x, y-1))^2/4 \end{aligned} \tag{25}$$

Under the hypothesis that $E(u)$ is constant in the 4-neighborhood of (x, y) and that pixel intensities are independently distributed, $(\bar{u}(x+1, y) - \bar{u}(x-1, y))/2$ has 0-mean and variance $\text{Var}(u(x, y, t))/(2T)$. Therefore, under a Gaussian distribution assumption, $2T\|\nabla\bar{u}\|^2/\text{Var}(u(x, y, t))$ follows a χ^2 law with two degrees of freedom.

We consequently eliminate pixels such that the p -value of $2T\|\nabla\bar{u}\|^2/\bar{\sigma}_u^2$ under this probability distribution is below 1%, that is, the former quantity must be smaller than 9.21 to keep the pixels.

We eventually discard pixels of coordinates (x, y) as soon as one of the intensity values in the time series $u(x, y, t)$ equals the lowest or highest possible gray level output (the range being 2^b , where b is the bit-depth). This procedure removes clipped pixels and defective pixels (hot or dead photosites).

3.2 Flicker reduction

The proposed flicker reduction procedure consists first in estimating γ_t for any t . The intuition is that $gp(x, y) + \mu$ is much larger than μ and δ for large intensity values, enabling further simplification. Indeed, let $v(x, y, t)$ be the ratio between the intensity and the average intensity of a given pixel:

$$v(x, y, t) = \frac{u(x, y, t)}{\bar{u}(x, y)} \quad (26)$$

This simplifies into

$$v(x, y, t) \simeq \frac{g\eta_{(1+\gamma_t)p(x,y)} + \delta(x, y)}{gp(x, y) + \mu} \simeq \frac{\eta_{(1+\gamma_t)p(x,y)}}{p(x, y)} \quad (27)$$

which is a random variable of mean $1 + \gamma_t$ and variance $(1 + \gamma_t)/p(x, y) \simeq 1/p(x, y)$. Consequently, this quantity should give an estimation of $1 + \gamma_t$.

A more accurate estimation is actually available. If X and Y are random variables, a Taylor expansion of X/Y around $(E(X), E(Y))$ gives the following approximations:

$$\begin{cases} E\left(\frac{X}{Y}\right) \simeq \frac{E(X)}{E(Y)} - \frac{\text{Cov}(X, Y)}{E(Y)^2} + \frac{E(X)\text{Var}(Y)}{E(Y)^3} \\ \text{Var}\left(\frac{X}{Y}\right) \simeq \frac{\text{Var}(X)}{E(Y)^2} - \frac{2E(X)\text{Cov}(X, Y)}{E(Y)^3} + \frac{E(X)^2\text{Var}(Y)}{E(Y)^4} \end{cases} \quad (28)$$

Here, with the time-independence assumption,

$$\begin{cases} E(u | \gamma_t) = g(1 + \gamma_t)p + \mu \\ \text{Var}(u | \gamma_t) = g^2(1 + \gamma_t)p + \sigma^2 \\ E(\bar{u} | \gamma_t) = \frac{1}{T} \sum_{t=1}^T (g(1 + \gamma_t)p + \mu) = g(1 + \bar{\gamma})p + \mu \\ \text{Var}(\bar{u} | \gamma_t) = \frac{1}{T} (g^2(1 + \bar{\gamma})p + \sigma^2) = \mathcal{O}(1/T) \\ \text{Cov}(u, \bar{u} | \gamma_t) = \frac{1}{T} \text{Var}(u | \gamma_t) = \mathcal{O}(1/T) \end{cases} \quad (29)$$

Since $E(\gamma_t) = 0$, we can further simplify with $\bar{\gamma} = \mathcal{O}(1/T)$. Substituting the expressions (29) in (28) and keeping only the most influencing terms lead to

$$\begin{cases} E(v | \gamma_t) &= \frac{g(1+\gamma_t)p+\mu}{g(1+\mathcal{O}(1/T))p+\mu} + \mathcal{O}(1/T) \\ &= \frac{1+\gamma_t+\mu/(gp)}{1+\mu/(gp)} + \mathcal{O}(1/T) \\ \text{Var}(v | \gamma_t) &= \frac{g^2(1+\gamma_t)p+\sigma^2}{(g(1+\bar{\gamma})p+\mu)^2} + \mathcal{O}(1/T) \\ &= \frac{g(1+\gamma_t)E(u)+\sigma^2-g(1+\gamma_t)\mu}{E(u)^2} + \mathcal{O}(1/T) \end{cases} \quad (30)$$

We can see from (30) that, for large values of the average gray level $E(u) = gp + \mu$, $E(v | \gamma_t)$ is an approximation of $1 + \gamma_t/(1 + \mu/(gp))$ with a minimum variance. Moreover, an estimation

of $E(v(x, y, t) | \gamma_t)$ is given by averaging $v(x, y, t)$ over a set of pixels for which $\bar{u}(x, y)$ is constant. This motivates the definition of the set

$$\mathcal{S}^* = \{(x, y), u^* - 3\sigma_{u^*} \leq \bar{u}(x, y) \leq u^* + 3\sigma_{u^*}\} \quad (31)$$

where u^* is the 99% quantile in the empirical intensity distribution of the averaged image $\bar{u} = gp + \mu + \mathcal{O}(1/T)$, and σ_{u^*} is the associated standard deviation. We assume that $\bar{u}(x, y, t)$ is constant over \mathcal{S}^* , equal to u^* . An estimation of $E(v(x, y, t) | \gamma_t)$ is then computed as a sample mean over the set \mathcal{S}^* .

Indeed, for any t ,

$$v^*(t) = \frac{1}{\#\mathcal{S}^*} \left(\sum_{(x,y) \in \mathcal{S}^*} v(x, y, t) \right) \quad (32)$$

is a random variable of expectation and variance

$$\begin{cases} E(v^*(t)) = \frac{1+\gamma_t+\mu/(u^*-\mu)}{1+\mu/(u^*-\mu)} + \mathcal{O}(1/T) \\ \text{Var}(v^*(t)) = \mathcal{O}(1/\#\mathcal{S}^* + 1/T\#\mathcal{S}^*) \end{cases} \quad (33)$$

where $\#\mathcal{S}^*$ denotes the cardinality of \mathcal{S}^* .

For the sake of simplicity, the mentions to $\mathcal{O}(1/T)$ and $\mathcal{O}(1/\#\mathcal{S}^*)$ are skipped in the remainder of this section. It amounts to assuming that the number of stacked images and the size of \mathcal{S}^* are large enough.

Once $v^*(t)$ has been calculated, the quantity defined for any (x, y, t) by $\tilde{u}(x, y, t) = u(x, y, t) - v^*(t)\bar{u}(x, y)$ is such that:

$$\begin{cases} E(\tilde{u}(x, y, t) | \gamma_t) &= g(1 + \gamma_t)p(x, y) + \mu \\ &\quad - \left(\frac{1+\gamma_t+\mu/(u^*-\mu)}{1+\mu/(u^*-\mu)} \right) (gp(x, y) + \mu) \\ &= g\gamma_t p(x, y) - \gamma_t \frac{u^*-\mu}{u^*} (gp(x, y) + \mu) \\ &= -\gamma_t \frac{\mu}{u^*} (u^* - \mu - gp(x, y)) \\ \text{Var}(\tilde{u}(x, y, t) | \gamma_t) &= g^2(1 + \gamma_t)p(x, y) + \sigma^2 \end{cases} \quad (34)$$

Let $K = E(\tilde{u}(x, y, t) | \gamma_t) / (E(v^*(t)) - 1)$. One has

$$K = -\frac{\mu}{u^*} (u^* - \mu - gp(x, y)) \frac{u^*}{u^* - \mu} \quad (35)$$

$$= -\mu \left(1 - \frac{gp(x, y)}{u^* - \mu} \right) \quad (36)$$

We can see that K does not depend on t . For a fixed $p(x, y)$, there is thus a proportionality relation between $E(\tilde{u}(x, y, t) | \gamma_t)$ and $E(v^*(t)) - 1$ for every t . This proportionality coefficient can be estimated by linear regression. As explained earlier, $E(v^*(t))$ is obtained by non-local estimation over the set \mathcal{S}^* . Similarly we choose an iso-value set to estimate, for every t , $E(\tilde{u}(x, y, t) | \gamma_t)$. We can see in (34) that the smallest value of $\text{Var}(\tilde{u}(x, y, t) | \gamma_t)$ is attained for small $p(x, y)$. We thus define the set

$$\mathcal{S}_* = \{(x, y), u_* - 3\sigma_{u_*} \leq \bar{u}(x, y) \leq u_* + 3\sigma_{u_*}\} \quad (37)$$

where u_* is the 1% quantile in the intensity distribution of the averaged image $\bar{u}(x, y)$, and σ_{u_*} the associated standard deviation. In the same way as v^* , an estimation of $E(\tilde{u}(x, y, t) | \gamma_t)$ for (x, y) such that $gp(x, y) = u_* - \mu$ is given by

$$v_*(t) = \frac{1}{\#\mathcal{S}_*} \left(\sum_{(x,y) \in \mathcal{S}_*} \tilde{u}(x, y, t) \right) \quad (38)$$

Finally a linear regression on the scatter plot $(v^*(t) - 1, v_*(t))$ gives an estimation of K . This permits us to obtain estimations of μ and γ_t . Indeed, from (36),

$$K = -\mu \left(1 - \frac{u_* - \mu}{u^* - \mu} \right) \quad (39)$$

hence $K(u^* - \mu) = -\mu(u^* - u_*)$ and:

$$\mu = \frac{K u^*}{K - u^* + u_*} \quad (40)$$

With this estimation of μ , we deduce by identifying v^* and its expectation given by (33) that

$$\tilde{\gamma}(t) = (v^*(t) - 1) \left(1 + \frac{\mu}{u^* - \mu} \right) \quad (41)$$

is an estimator of γ_t for every t .

With these estimations of γ_t and μ , identified in the remainder of the section with their actual values, we can define:

$$\hat{u}(x, y, t) = u(x, y, t) - (1 + \gamma_t)(\bar{u}(x, y) - \mu) \quad (42)$$

This quantity is such that:

$$E(\hat{u}) = E(E(\hat{u} | \gamma_t)) = E(\mu) = \mu \quad (43)$$

and:

$$\text{Var}(\hat{u}) = E(\text{Var}(\hat{u} | \gamma_t)) + \text{Var}(E(\hat{u} | \gamma_t)) \quad (44)$$

$$= E(g^2(1 + \gamma_t)p + \sigma^2 + (1 + \gamma_t)^2 \text{Var}(\bar{u})) + \text{Var}(\mu) \quad (45)$$

$$= g^2p + \sigma^2 + (1 + \sigma_\gamma^2) \text{Var}(\bar{u}) \quad (46)$$

$$= gE(u) + \sigma^2 - g\mu + (1 + \sigma_\gamma^2) \text{Var}(\bar{u}(x, y)) \quad (47)$$

Since $\text{Var}(\bar{u}(x, y)) = \mathcal{O}(1/T)$, we can write the following affine relation between the variance of the flicker-removed stack $\hat{u}(x, y, t)$ and the expected value of $u(x, y, t)$ (which is not affected by the light flickering):

$$\text{Var}(\hat{u}(x, y, t)) = gE(u(x, y, t)) + \sigma^2 - g\mu \quad (48)$$

which is the same relation as in the standard model (3).

Remark 1. In practice, each term of the sum in the definition (32) of v^* is weighted by $e^{-(\bar{u}(x, y) - u^*)^2 / (2\sigma_{u^*}^2)}$, and similarly for v_* in the definition (38). This acts as a soft threshold in the definition of \mathcal{S}^* or \mathcal{S}_* as noted in another context in [18]. By construction, $v^*(t)$ and $v_*(t)$ are non-local estimators [11].

Remark 2. Since very small values for γ_t yield $E(v^*(t)) - 1 \simeq E(v_*(t)) \simeq 0$, (cf. (33-34) with $\gamma_t \simeq 0$), the accuracy of the estimated μ obtained through linear regression should be all the higher as the standard deviation σ_γ is large.

Remark 3. The choice of the 99%/1% quantiles proves to give satisfactory results in all experiments of Section 4. However, these values can be slightly altered if, in particular images, the cardinality of the sets \mathcal{S}^* or \mathcal{S}_* is not large enough.

3.3 Linear regression

From (48), a simple linear regression over the scatter plot of the time sample variance of the $\hat{u}(x, y, t)$ against the time sample mean of the $u(x, y, t)$ gives us estimations of the slope g and intercept $\sigma^2 - g\mu$, hence an estimation of σ since μ is known at this stage by (40).

Once γ_t and μ have been estimated, another possibility could have been to plug these values in the coefficients of (24) estimated through quadratic regression, in order to get estimations of g and σ . We have noted that the obtained estimations were not as good as those obtained by linear regression with (48), probably because of the more pronounced effect of PRNU due to the quadratic term and of the correlation between the linear and the quadratic term. We therefore do not use this quadratic regression to estimate the camera parameters. The result of this regression is, however, used to obtain an estimation of the covariance matrix $\text{Cov}(\alpha, \beta)$.

3.4 Summary: algorithm

While simple linear regression permits us to estimate the camera parameters g , μ , σ and σ_γ^2 as described above, multiple linear regression with (23) (not restricted to pixels unaffected by vibrations) gives additionally an estimation of the covariance matrix of the joint process (α_t, β_t) . The whole procedure is summarized in Algorithm 1.

Input: A series of T raw images $u(x, y, t)$ of a static scene affected by a flickering light and possibly by vibrations.

1. Compute sample expectation $\bar{u}(x, y)$ and sample variance $\bar{\sigma}_u^2$ at every pixel. (Section 2.3)
2. Remove clipped pixels and pixels such that $2T\|\nabla\bar{u}\|^2/\bar{\sigma}_u^2 > 9.21$. (Section 3.1)
3. For every t , compute $v^*(t)$ (eq. (32)) and $v_*(t)$ (eq. (38)). A linear regression on the scatter plot $(v_*(t), v^*(t) - 1)$ gives the slope K (eq. (36)), and subsequently estimations of μ (eq. (40)) and of γ_t for every $1 \leq t \leq T$ (eq. (41)), hence σ_γ^2 .
4. A linear regression between the sample variance of $\hat{u}(x, y, t)$ (eq. (42)) and the sample expectation of $u(x, y, t)$ gives a slope of g and an intercept of $\sigma^2 - g\mu$ (eq. (48)), hence an estimation of the camera parameters g , $\sigma^2 - g\mu$, σ .

Independently, an estimation of the covariance matrix of the vibration process (α_t, β_t) is obtained from eq. (23) by a multiple linear regression between $\bar{\sigma}_u^2$ and \bar{u}^2 , \bar{u} , $(\partial\bar{u}/\partial x)^2$, $(\partial\bar{u}/\partial y)^2$, and $\partial\bar{u}/\partial x \cdot \partial\bar{u}/\partial y$ (performed on the whole data set, including pixels affected by vibrations).

Output: An estimation of $g, \mu, \sigma, \sigma^2 - g\mu, \gamma_t, \text{Cov}(\alpha, \beta)$, and σ_γ .

Algorithm 1: Estimation of the camera parameters and of the external parameters by stacking images affected by illumination flickering and vibrations.

3.5 Balancing the rolling shutter effect

In any digital single-lens reflex (DSLR) camera with a focal-plane shutter, pixels are not illuminated simultaneously. Such a shutter is indeed made of two curtains running one after the other across the sensor plane. This is all the more noticeable when fast shutter speeds are used, especially with speeds faster than X-sync, defined as the fastest shutter speed at which the whole sensor is completely exposed. This feature, illustrated in Figures 2 and 3, gives so-called rolling shutter effects. CMOS cameras with an electronic shutter are also affected since the image is not captured instantaneously but instead row by row. The rolling shutter effect does not change the

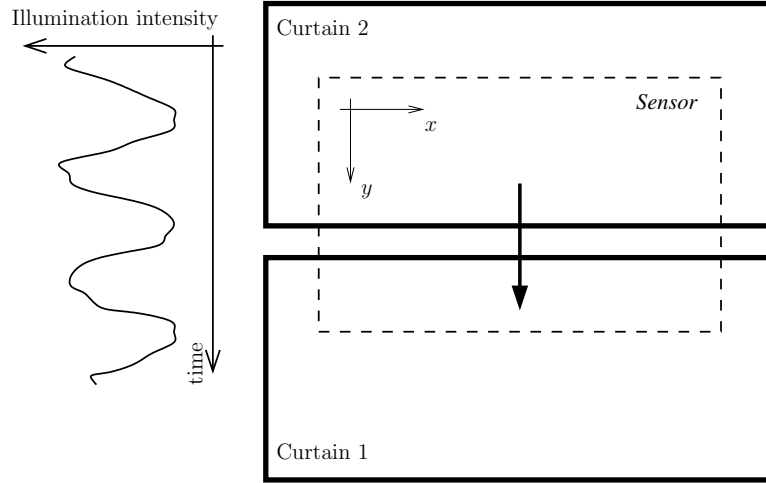


Figure 2: Illustration of the rolling shutter effect: the two curtains go from the top to the bottom, uncovering a part of the sensor. If the scene is illuminated by a flickering source, the illumination intensity varies during the travel of the curtains.

quadratic relation of (24) which only involves the variance σ_γ^2 and is based on a local argument, but this makes ineffective the image-wide estimation of each γ_t in Section 3.2.

The proposed workaround consists in considering that γ_t depends on the row y (since the DSLR of Section 4, as most DSLR, have vertical-travel shutters). The expectation of $v^*(t)$ defined in (32) is now

$$E(v^*(t)) = \frac{1 + \frac{1}{\#\mathcal{S}^*} \sum_{(x,y) \in \mathcal{S}^*} \gamma_t(y) + \mu/(u^* - \mu)}{1 + \mu/(u^* - \mu)} \quad (49)$$

and the expectation of $v_*(t)$ defined in (38) is

$$E(v_*(t)) = - \left(\frac{1}{\#\mathcal{S}_*} \sum_{(x,y) \in \mathcal{S}_*} \gamma_t(y) \right) \frac{\mu}{u^*} (u^* - u_*) \quad (50)$$

The ratio between $v_*(t)$ and $v^*(t) - 1$ is now

$$- \frac{\#\mathcal{S}^* \sum_{(x,y) \in \mathcal{S}_*} \gamma_t(y)}{\#\mathcal{S}_* \sum_{(x,y) \in \mathcal{S}^*} \gamma_t(y)} \mu \left(1 - \frac{u_* - \mu}{u^* - \mu} \right) \quad (51)$$

instead of K given by (39). Generally speaking, since the sets \mathcal{S}^* and \mathcal{S}_* differ, this quantity is likely to be a biased estimation of K , giving a biased estimation of μ . However, if the distribution along y of both sets is alike, then the ratio $\frac{\#\mathcal{S}^* \sum_{(x,y) \in \mathcal{S}_*} \gamma_t(y)}{\#\mathcal{S}_* \sum_{(x,y) \in \mathcal{S}^*} \gamma_t(y)}$ is close to 1. Even in the limit case where \mathcal{S}^* and \mathcal{S}_* form two clusters with a large illumination difference, the distribution along time t of the introduced bias is likely to be symmetrically distributed around 1, and should be consequently smoothed out by the linear regression over $(v^*(t) - 1, v_*(t))$ used to estimate K , then μ . Consequently, even for fast shutter speed, we keep on using the image-wide procedure of Section 3.2 to estimate μ , which gives good experimental results.

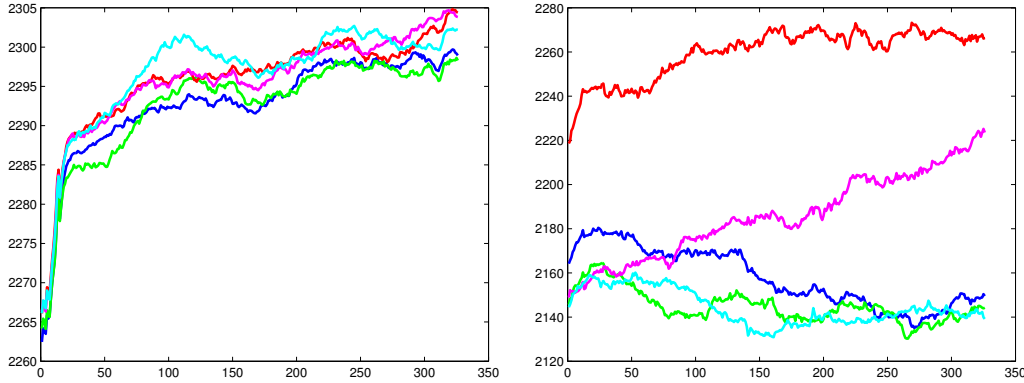


Figure 3: Illustrating the rolling shutter effect affecting a DSLR with a vertical-travel shutter under a neon tube light. The profile of the pixel intensity $u(x, y)$ along a fixed x is shown, for five images taken with a static camera at different times (in abscissa y , in ordinate $u(x, y)$, each image gives a colored curve). The profiles are smoothed with a moving average to decrease the effect of noise. Left: ISO 100, $1/3$ s exposure time; Right: ISO 6400, $t = 1/320$ s exposure time. X-sync is here $1/160$ s. While the profiles in the low speed case are almost superimposed, except for a slight translation explained by a varying illumination, the profiles in the high speed case are very different. Not only is the illumination flickering more pronounced in this latter case (this is due to the shorter integration time), explaining the larger vertical translations of the five profiles, but the profiles also change from image to image. This phenomenon is explained by a significant change in the illumination intensity between the top and the bottom of the image during the travel of the shutter.

We adapt, however, the estimation of γ_t from Section 3.2 and we use, instead of (32), the modified non-local estimator $v^*(y, t)$

$$v^*(y, t) = \frac{1}{N_y \#\mathcal{S}^*} \left(\sum_{(x', y') \in \mathcal{S}^*} e^{-(y'-y)^2 / (2\sigma_y^2)} v(x', y', t) \right) \quad (52)$$

with a normalization term $N_y = \sum_{(x', y') \in \mathcal{S}^*} e^{-(y'-y)^2 / (2\sigma_y^2)}$. This amounts to estimating $\gamma_t(y)$ on horizontal strips of a fixed width centered at row y . We take $\sigma_y = 50$ pixels. Of course, a rigorous setting of the width should involve the flickering frequency, the shutter speed, and the sensor y -size (or the y -size of a cropped image). We leave it for a future work.

We obtain an estimation of $\gamma_t(y)$ from (41), which is then plugged into (42) and the same computation as in (43-47) still gives the affine relation (48).

4 Experimental results

The aim of this section is to assess the proposed estimation method from a series of images under the same lens aperture, shutter speed, and ISO setting. The algorithm of Figure 1 gives an estimation of the covariance matrix of the vibration process (α_t, β_t) , the relative fluctuation of the light intensity γ_t , and the parameters governing the noise model, namely the gain g , the offset μ and the read-out noise σ . This section proves that satisfactory estimations can be obtained, thanks to illumination flickering. A comparison with the software provided by A. Foi¹ (implementing [24] and based on the analysis of a single image, consequently not affected by flickering and vibrations) which gives estimations of g and $\sigma^2 - g\mu$ is also provided. In order to compare estimations on the same amount of data, this software is run on a composite image where all T images from the stack have been placed in a $\sqrt{T} \times \sqrt{T}$ mosaic. The default parameters are used.

Section 4.1 details a running example. Section 4.2 presents results for a synthetic data set. Section 4.3 gives results for actual raw data from a PCO Sensicam QE camera and two Canon EOS DSLR cameras, namely the old EOS 350D and the recent EOS 6D. A comparison with the results of the photon transfer method is also given. For visualization purpose, the contrast of the linear raw images has been modified in the figures. The camera parameters are given in “gray-level” units as in [3].

4.1 Running example

Figure 4 shows an illustrative example. $T = 100$ images of an X-Rite Colorchecker illuminated by a neon tube light are taken with a Canon EOS 6D camera (row “ISO 6400” in Table 5, hence a fast shutter speed, prone to the rolling shutter effect). The scatter plot of $v_*(t)$ against $v^*(t) - 1$ shows the linear relation of slope $K < 0$. In this case, the assumptions of Section 3.5 prove to be satisfied, the linear relation is nearly perfect. The light flickering $1 + \gamma_t(y)$ is estimated and $\sigma_\gamma = 0.24$ is found (see Table 9). The dependence of $\gamma_t(y)$ on y is noticeable. The graph of the sample variance of $u(x, y, t)$ against the sample expectation has a quadratic trend as predicted by (24). The plot for $\tilde{u}(x, y, t)$ is not linear when γ_t is assumed constant over the image: pixels belonging to some color patches are not adequately corrected, which explains the clusters out of the linear trend noticed on the lower part of the graph. In this case, the regression line does not give a slope and an intercept consistent with the values of the gain, offset, and read-out noise. With an estimation performed as in Section 3.5, the trend becomes linear and a correct estimation of the camera parameters is possible (see Section 4.3). The green points are outliers discarded by the first step of the algorithm (pixels affected by vibrations, see Section 3.1), and the estimations of the camera parameters are based on the blue points.

¹v. 2.31, available at <http://www.cs.tut.fi/~foi/sensornoise.html>

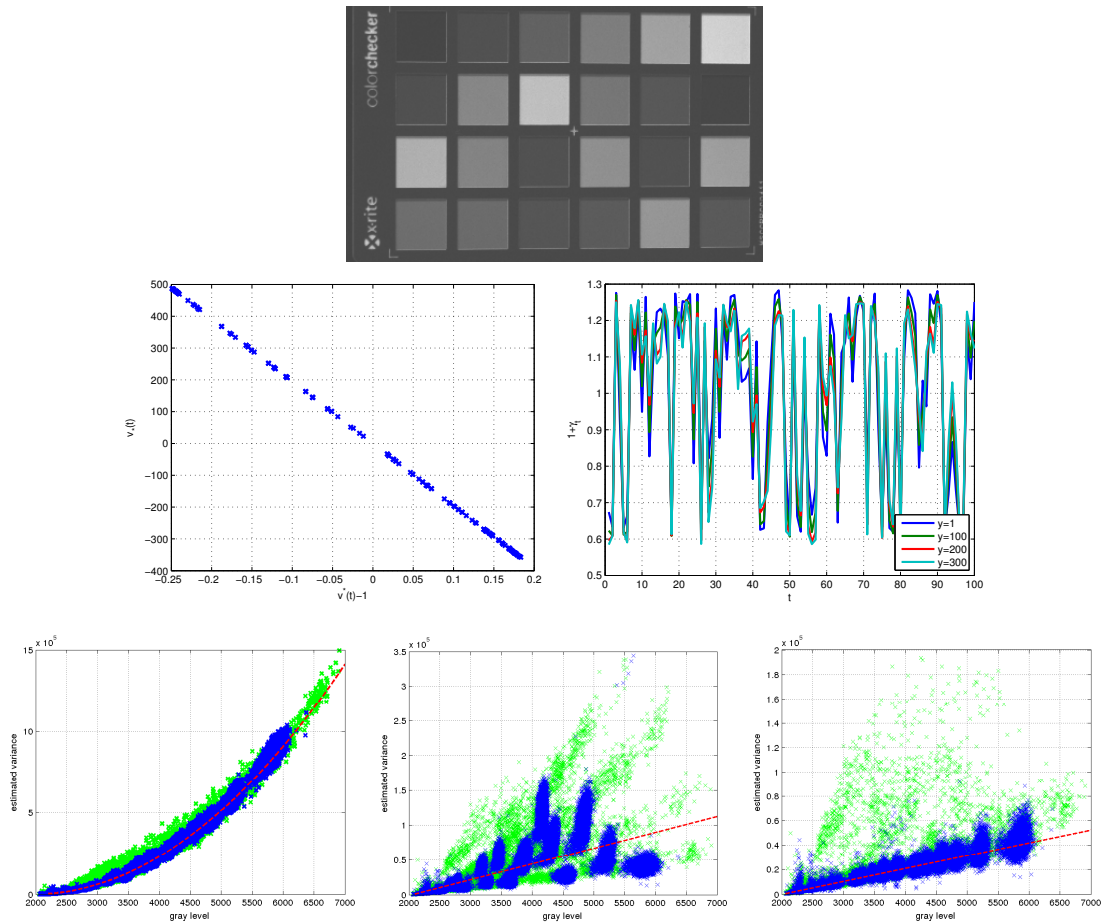


Figure 4: Running example. On the top: an image from the series. In the middle: graph of $v_*(t)$ against $v^*(t) - 1$, and estimation of the relative fluctuation of the light $1 + \gamma_t(y)$ for several values of y . On the bottom: graph of the sample variance of $u(x, y, t)$ against the sample mean of $u(x, y, t)$; graph of the sample variance of $\hat{u}(x, y, t)$ against the sample mean of $u(x, y, t)$ (image-wide estimation); the same statistics after local estimation (to balance rolling shutter effect).

camera	A	B	C	exp.	1	2	3
A	600	3,000	10,000	σ_γ	0.1	0.01	0.05
g	5	1	0.3	σ_α	0.3	0.1	0.01
μ	200	100	40	σ_β	0.2	0.05	0.02
σ	15	8	3				

Table 1: Parameter values: camera settings on the left, and experimental conditions on the right.

4.2 Synthetic data

In this experiment, stacks of images are generated from reference images using the model of (4). More precisely, $p(x, y)$ is the intensity value of a 512×512 reference image scaled to $[0, A]$, where $A > 0$ is the maximum number of generated electrons at a given photosite. For every t , α_t , β_t and γ_t are independent random numbers simulated following a Gaussian distribution of standard deviation equal to, respectively, σ_α , σ_β , and σ_γ . The value of $p(x + \alpha_t, y + \beta_t)$ is obtained by linear interpolation of the scaled reference image p (a Gaussian blur of standard deviation 0.5 pixel is first applied to the reference images to simulate optical blur). A stack $u(x, y, t)$ of T images is randomly generated from the Poisson-Gaussian model of (4) and quantized over 12 bits afterward. Note that quantization irremediably leads to loss of information. It should also be noted that the intensity $p(x, y)$ may come from a noisy reference image. This feature does not play any role in our estimation process, since this noisy component is static and does not change along the stack. This may however give an additional bias in the estimation by the software implementing [24].

Since the results vary between realizations of the stochastic processes, fifty such simulations are run, which permits us to estimate mean values together with their standard deviation. In the remainder of this section we give the mean \pm twice the standard deviation obtained in this Monte Carlo approach.

Three camera models and three external conditions are tested, which gives nine different experimental settings for a given reference image. The corresponding parameter values are in Table 1. Synthetic cameras A to C have typical noise levels for varying ISO values of a 12-bit camera. Parameter A is set so that the quantized intensity values span the 12-bit range. In Table 1, the range of the vibration and flickering amplitudes correspond to typical observations. For example, the vibration amplitude in external conditions 3 correspond to the experimental measurements in [55]. External conditions 1 are very demanding, with vibrations whose amplitude are likely to be as large as one pixel, and large illumination changes between successive images.

Six reference images are tested, see Figures 5 and 5. The first one is a synthetic calibration target with large homogeneous areas (Synthetic). The others come from the USC-SIPI Image Database². As we shall see, the Synthetic image image is well adapted to Foi's software. Nevertheless, our method also needs iso-value sets for the non-local estimation of Section 3.2 (cf the 99% quantile level set in (32) and the 1% quantile level set in (38)), and the images should be smooth enough so that pixels are not overly removed because of large gradients. The remaining reference images are chosen to test the influence of irregular textures. Such textures not only make it difficult to segment the image, but also give a larger proportion of pixels affected by the vibrations (for instance, 59.1% for Boat against 8.8% for Synthetic, in the sense of Section 3.1).

A first experiment consists in assessing the influence of the number T of stacked images. Figure 7 shows the typical evolution of the relative precision of the estimated parameters together with their 95% confidence intervals (\pm twice the standard deviation of the estimation, shaded

²available at <http://sipi.usc.edu/database/>

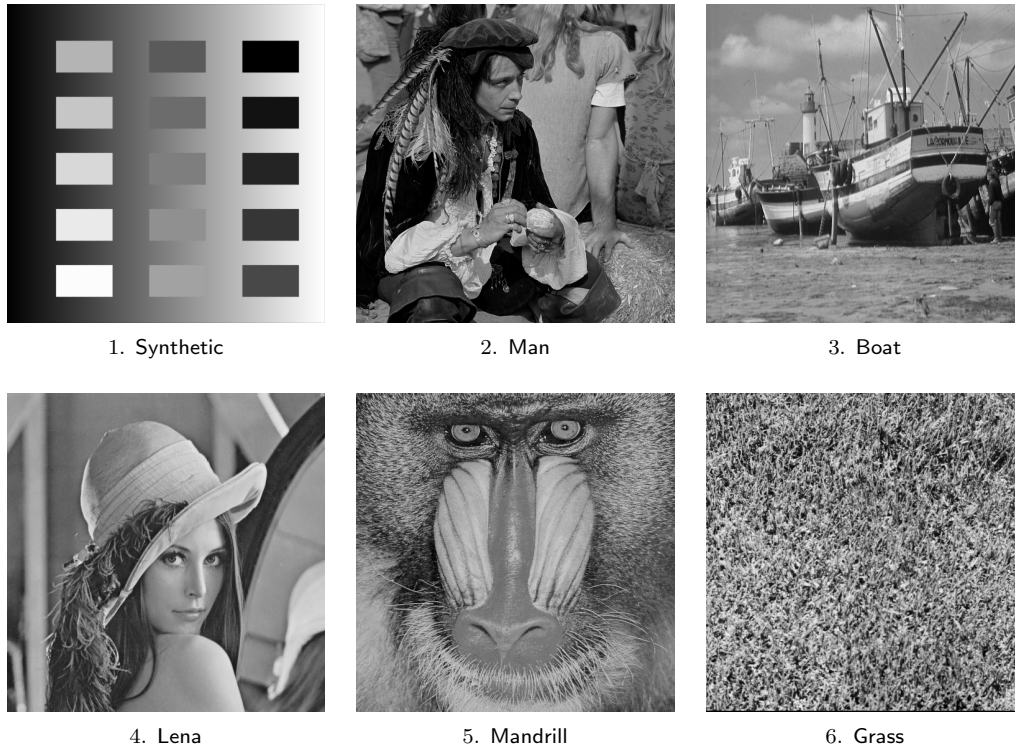


Figure 5: Reference images, with an increasing high-frequency texture content. These images have a size of 512×512 pixels, except for Man which has a size of 1024×1024 pixels.

plots in the figure). The reference image is here the synthetic target. Here “relative precision” means that the values of interest are divided by the ground truth value. The estimated confidence intervals show a $1/\sqrt{T}$ decrease as in every Monte Carlo approach. This is, however, limited by the quantization of the data which imposes a lower bound to the accuracy (see, e.g., [58]). From these results, the parameter T is set to 100 in the remainder of the report. As we can see, a smaller number of stacked images would also give acceptable results.

Table 2 gives the comprehensive results for the **Synthetic** reference image, and Table 3 for the **boat** image. The first row gives the experiment number. Experiment “X n” deals with the camera “X” in the experimental conditions “n” in Table 1. For each of the estimated parameter (in column), the ground truth (GT) is given, as well as the result of the proposed algorithm (estim.), and for g and $\sigma^2 - g\mu$ the output of the software by Foi et al.

We can see that with the **Synthetic** reference image, all parameters are very accurately estimated and the actual values are almost always in the confidence interval of the estimation. Large vibrations (conditions 1) give less accurate estimations of the slope $\sigma^2 - g\mu$ and consequently of σ . The results of the software provided by A. Foi are comparable, and, of course, are not affected by flickering or vibrations. This experiment proves that, with a simple synthetic image stack, the proposed approach allows us to accurately estimate not only the camera parameters g , μ , σ but also the external parameters of the experimental setting, namely σ_γ , σ_α , and σ_β , benefiting from illumination flickering.

The textured **boat** reference image is more challenging. On the one hand we can see that, in

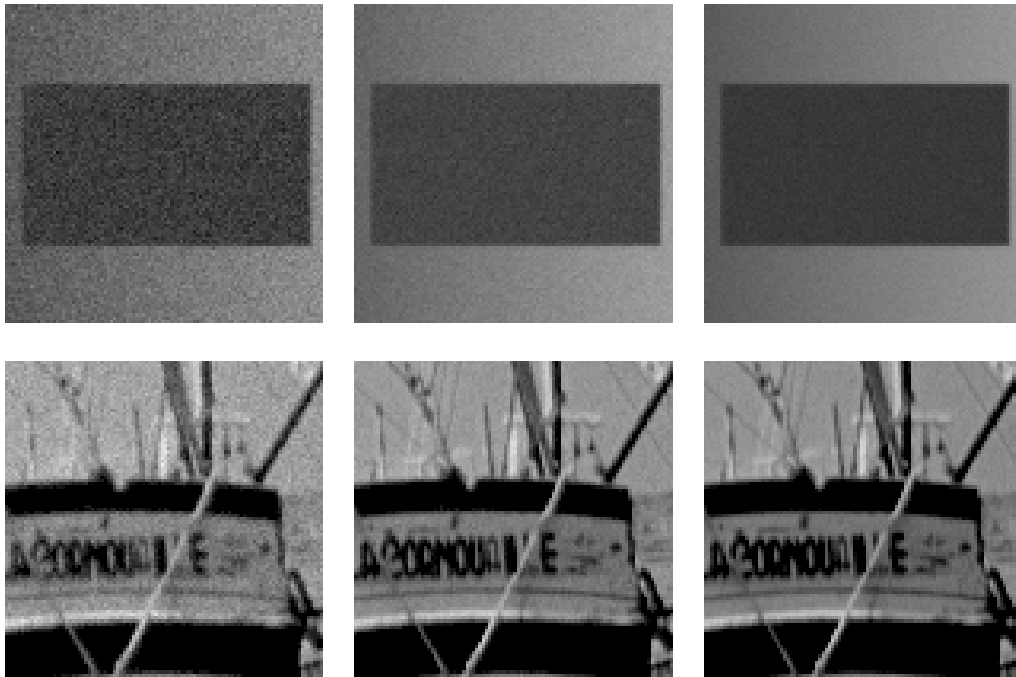


Figure 6: Close-up of the 12-bit output of the three cameras A , B , C for the synthetic and boat reference images. (Best viewed in the pdf file.)

this case, the performance of the method by Foi et al. deteriorates. For some textured reference image, its results are even totally wrong. It should be noted that a robust version of their algorithm has been recently proposed [6]. On the other hand, the proposed algorithm gives quite reliable estimations of g (the actual value is within the estimated confidence interval, which is quite small). The variability of the estimated μ is very large in case 2 (with $\sigma_\gamma = 0.01$), as expected from Remark 2 in Section 3.2. Concerning the estimation of $\sigma^2 - g\mu$ (and consequently of σ) the vibrations strongly affect the accuracy and the variability. However, a reliable estimation is still obtained in case 3 (moderate vibrations). Note that in all cases, the estimation of the light variability σ_γ is very good, and the estimation of the variability σ_α and σ_β of the vibrations are quite accurate, even with strong vibrations (cases 1 and 2).

Figures 8 and 9 show the error bars (95% confidence intervals) for the estimation of the intrinsic parameters g , μ , $\sigma^2 - g\mu$ and σ , and of the extrinsic parameters σ_γ , σ_α , and σ_β , respectively. Concerning the intrinsic parameters in Figure 8, we can see that the estimation of the gain deteriorates in the case of high-frequency textures (reference images 5 and 6), especially for large vibrations (experimental condition 1). In other cases, the relative error is well below 10%. As predicted by the theory, the quality of the estimation of μ is poor for low σ_γ (condition 2), except for lightly textured images (reference images 1 and 2). The relative error is larger when μ decreases. The estimation of the slope $\sigma^2 - g\mu$ also deteriorates on textured images, and it is all the more noticeable as the vibration amplitude is large (condition 1). With tiny vibrations (condition 3), corresponding to more realistic cases, a reliable estimation is available in all cases, although the variability is large for textured images. The estimation of σ directly follows the estimation of $\sigma^2 - g\mu$. Concerning the extrinsic parameters in Figure 9, we can see that the

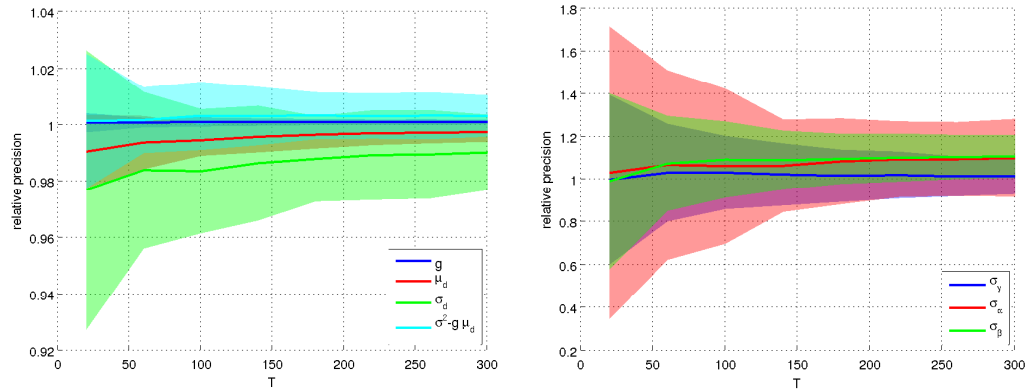


Figure 7: Evolution of the relative precision of the estimated parameters with respect to the number of stacked images (left: intrinsic parameters $g, \mu, \sigma, \sigma^2 - g\mu$: right: external parameters $\sigma_\gamma, \sigma_\alpha, \sigma_\beta$). Camera A is used with conditions 3 and the Synthetic target as reference image.

estimation of the flicker amplitude σ_γ is reliable in spite of a deterioration with textured images (reference image 6) in the case of small σ_γ (condition 2), and that the estimation of the vibration amplitude σ_α and σ_β are slightly overvalued, with unreliable estimation of extreme amplitudes (σ_α in condition 1) with the high gain camera A in the untextured reference image 1).

exp.		g	μ	σ	$\sigma^2 - g\mu$	σ_γ	σ_α	σ_β
A 1	GT	5	200	15	-775	0.1	0.3	0.2
	estim.	5.00 ± 0.03	200.1 ± 0.6	15.2 ± 0.4	-769.6 ± 15.7	0.10 ± 0.01	0.35 ± 0.07	0.23 ± 0.04
	Foi et al.	5.04 ± 0.02			-782.3 ± 7.6			
A 2	GT	5	200	15	-775	0.01	0.1	0.05
	estim.	5.00 ± 0.01	199.9 ± 4.6	15.0 ± 0.8	-775.3 ± 7.5	0.010 ± 0.01	0.11 ± 0.02	0.054 ± 0.007
	Foi et al.	5.04 ± 0.01			-781.1 ± 6.2			
A 3	GT	5	200	15	-775	0.05	0.01	0.02
	estim.	5.00 ± 0.01	200.0 ± 1.0	15.0 ± 0.3	-775.7 ± 10.3	0.050 ± 0.007	0.011 ± 0.003	0.022 ± 0.004
	Foi et al.	5.04 ± 0.02			-782.0 ± 6.9			
B 1	GT	1	100	8	-36	0.1	0.3	0.2
	estim.	1.00 ± 0.00	100.0 ± 0.3	8.2 ± 0.1	-33.6 ± 1.9	0.10 ± 0.02	0.28 ± 0.14	0.22 ± 0.05
	Foi et al.	1.01 ± 0.00			-36.6 ± 1.7			
B 2	GT	1	100	8	-36	0.01	0.1	0.05
	estim.	1.01 ± 0.00	99.6 ± 3.1	8.0 ± 0.2	-35.9 ± 2.3	0.010 ± 0.002	0.11 ± 0.02	0.054 ± 0.008
	Foi et al.	1.01 ± 0.00			-36.2 ± 1.7			
B 3	GT	1	100	8	-36	0.05	0.01	0.02
	estim.	1.00 ± 0.00	100.0 ± 0.6	8.0 ± 0.1	-36.0 ± 2.2	0.050 ± 0.007	0.011 ± 0.003	0.021 ± 0.003
	Foi et al.	1.01 ± 0.00			-36.3 ± 1.7			
C 1	GT	0.3	40	3	-3	0.1	0.3	0.2
	estim.	0.300 ± 0.000	40.0 ± 0.1	3.34 ± 0.13	-0.84 ± 0.88	0.098 ± 0.015	0.21 ± 0.05	0.21 ± 0.06
	Foi et al.	0.302 ± 0.001			-2.98 ± 0.26			
C 2	GT	0.3	40	3	-3	0.01	0.1	0.05
	estim.	0.300 ± 0.001	40.0 ± 1.1	3.00 ± 0.12	-3.03 ± 0.73	0.010 ± 0.001	0.11 ± 0.02	0.054 ± 0.009
	Foi et al.	0.302 ± 0.001			-2.97 ± 0.23			
C 3	GT	0.3	40	3	-3	0.05	0.01	0.02
	estim.	0.300 ± 0.000	40.0 ± 0.2	3.02 ± 0.10	-2.88 ± 0.62	0.050 ± 0.006	0.011 ± 0.003	0.022 ± 0.004
	Foi et al.	0.302 ± 0.001			-2.93 ± 0.34			

Table 2: Parameter estimation with the Synthetic reference image.

exp.		g	μ	σ	$\sigma^2 - g\mu$	σ_γ	σ_α	σ_β
A 1	GT	5	200	15	-775	0.1	0.3	0.2
	estim.	5.06 ± 0.02	200.3 ± 8.1	16.4 ± 1.6	-744 ± 28	0.10 ± 0.01	0.34 ± 0.06	0.21 ± 0.04
	Foi et al.	5.30 ± 0.05			-811 ± 68			
A 2	GT	5	200	15	-775	0.01	0.1	0.05
	estim.	5.02 ± 0.02	218.3 ± 85.2	16.5 ± 14.8	-780 ± 26	0.010 ± 0.001	0.11 ± 0.02	0.049 ± 0.008
	Foi et al.	5.43 ± 0.05			-844 ± 71			
A 3	GT	5	200	15	-775	0.05	0.01	0.02
	estim.	5.01 ± 0.02	198.7 ± 19.0	14.6 ± 3.3	-780 ± 31	0.050 ± 0.007	0.011 ± 0.01	0.019 ± 0.001
	Foi et al.	5.52 ± 0.05			-884 ± 75			
B 1	GT	1	100	8	-36	0.1	0.3	0.2
	estim.	1.05 ± 0.02	100.2 ± 3.2	10.7 ± 1.3	11 ± 30	0.10 ± 0.01	0.33 ± 0.09	0.21 ± 0.06
	Foi et al.	1.16 ± 0.03			-49.7 ± 36.0			
B 2	GT	1	100	8	-36	0.01	0.1	0.05
	estim.	1.02 ± 0.01	113.6 ± 131.1	7.6 ± 9.6	-44.1 ± 11.8	0.010 ± 0.002	0.11 ± 0.02	0.051 ± 0.007
	Foi et al.	1.28 ± 0.03			-69.8 ± 31.3			
B 3	GT	1	100	8	-36	0.05	0.01	0.02
	estim.	1.00 ± 0.01	100.3 ± 13.5	8.02 ± 1.13	-35.9 ± 11.1	0.050 ± 0.007	0.011 ± 0.006	0.020 ± 0.004
	Foi et al.	1.37 ± 0.02			-102 ± 31			
C 1	GT	0.3	40	3	-3	0.1	0.3	0.2
	estim.	0.345 ± 0.015	40.1 ± 2.4	7.96 ± 1.80	50.4 ± 28.8	0.010 ± 0.01	0.33 ± 0.10	0.20 ± 0.05
	Foi et al.	0.435 ± 0.022			-27.1 ± 31.8			
C 2	GT	0.3	40	3	-3	0.01	0.1	0.05
	estim.	0.326 ± 0.012	51.6 ± 136	2.63 ± 5.97	-9.22 ± 10.8	0.010 ± 0.001	0.11 ± 0.01	0.052 ± 0.007
	Foi et al.	0.558 ± 0.02			-44.0 ± 31.7			
C 3	GT	0.3	40	3	-3	0.05	0.01	0.02
	estim.	0.301 ± 0.002	40.1 ± 12.8	3.03 ± 0.97	-2.65 ± 3.90	0.050 ± 0.007	0.011 ± 0.006	0.019 ± 0.005
	Foi et al.	0.651 ± 0.016			-72.0 ± 26.9			

Table 3: Parameter estimation with the boat reference image.

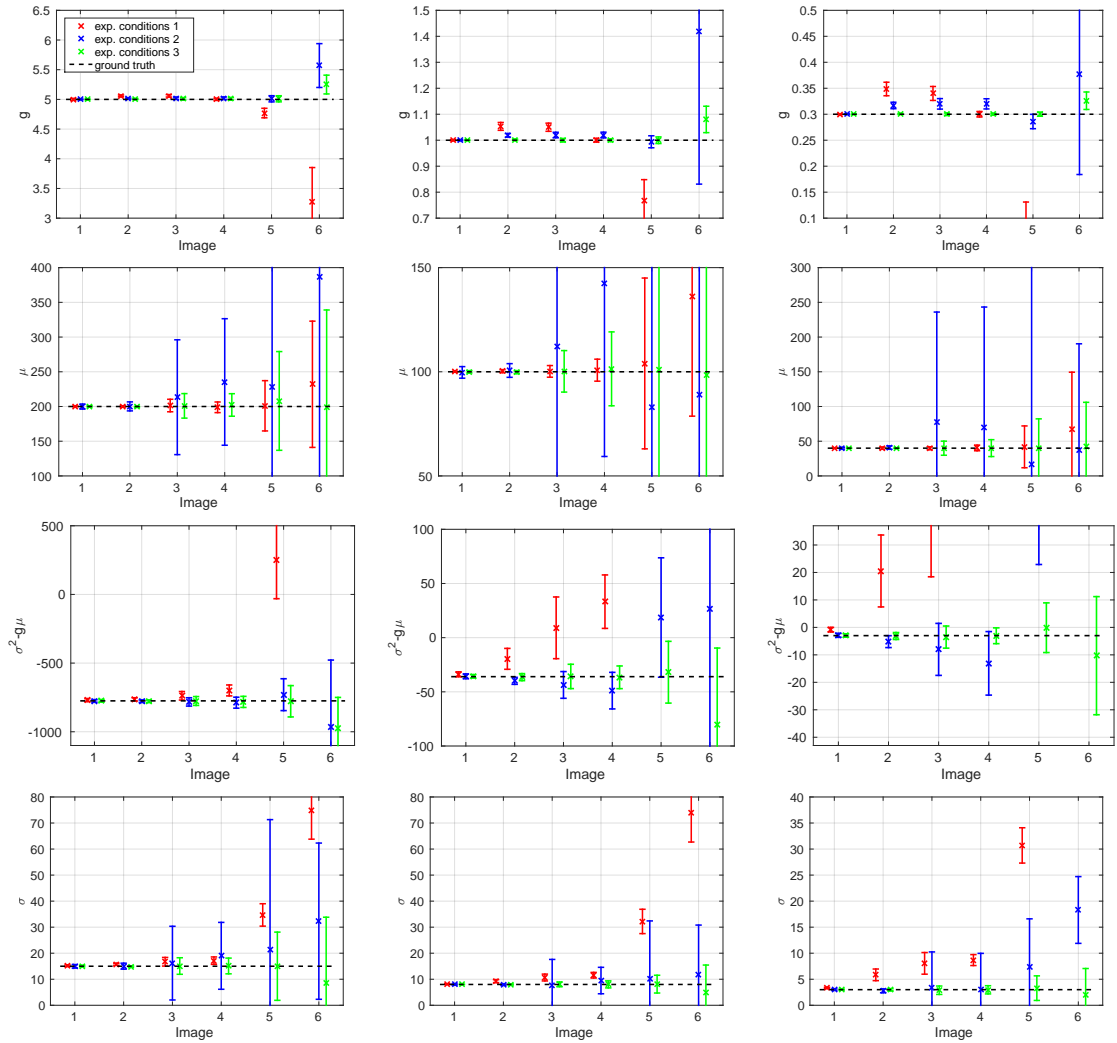


Figure 8: Estimation of the intrinsic camera parameters (g , μ , $\sigma^2 - g\mu$, and σ , from top to bottom) for camera A (left), camera B (middle), camera C (right), for each reference image 1 to 10. The caption for the top left plot holds for all of them.

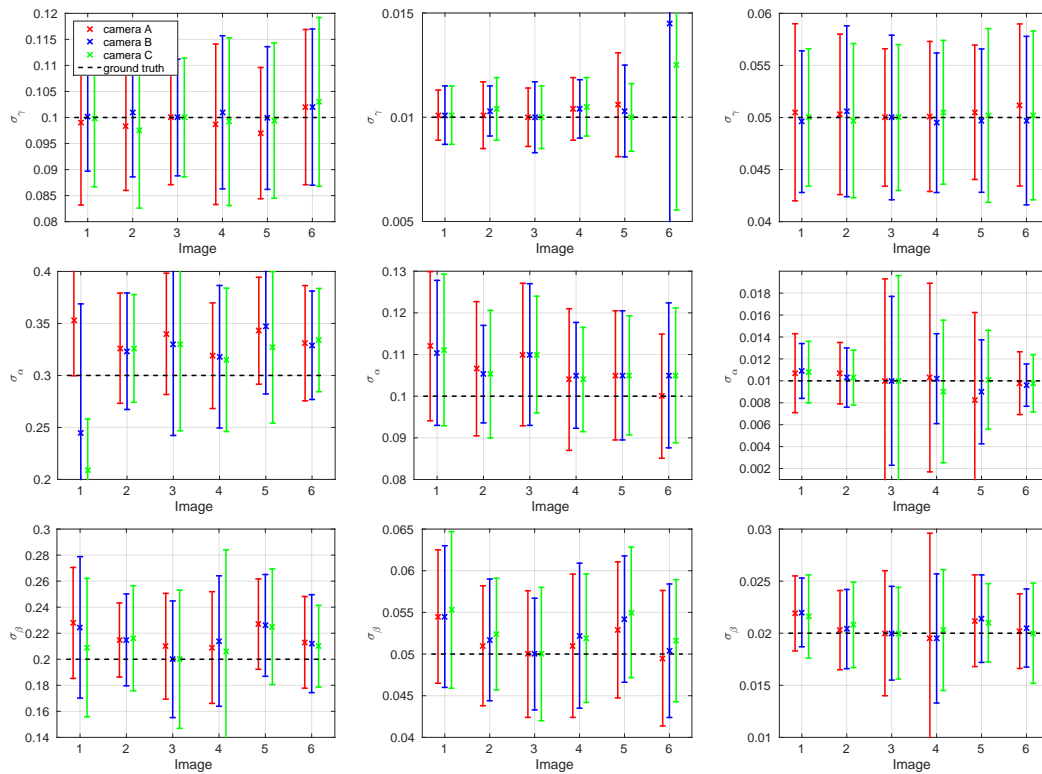


Figure 9: Estimation of the extrinsic parameters (σ_γ , σ_α , σ_β , from top to bottom) for condition 1 (left), condition 2 (middle), condition 3 (right), for each reference image 1 to 10. The caption for the top left plot holds for all of them.

4.3 Real data

In this section, image series from a PCO Sensicam QE and two Canon DSLR cameras are tested.

4.3.1 PCO Sensicam QE

Experiments are performed with a PCO Sensicam QE camera which gives 1040x1376 12-bit images. The gain parameter is set to “high”. This camera is equipped with a 105-mm Sigma macro lens. It is cooled to -12°C , and it has been shown that, for standard exposure times, the noise level is nearly constant (see, e.g., [33, p. 24-27] where it is shown that it is the case for exposures below 100ms.). Values for g , μ , and σ are provided by the manufacturer [1], supposedly following the EMVA procedure [3]: $g = 0.519$ (“gain high” mode), $\sigma = 1.15$, $\mu = 45.46$, hence $\sigma^2 - g\mu = -22.26$. In [52], we have estimated with an independent method $g = 0.528$ and $\sigma^2 - g\mu = -21.01$, hence close to the values given in the manufacturer’s datasheet.

Four series are taken, under a neon tube light. The exposure time is 13ms, and the image acquisition is triggered electronically, which gives a constant frequency. Let us note that this CCD camera is not prone to rolling shutter effect.

The estimation of the noise parameters is given in Table 4, with an estimation of the illumination flickering standard deviation σ_{γ} , and illustrations in Figures 10 to 13

		g	σ	μ	$\sigma^2 - g\mu$	σ_{γ}
	manufacturer [1]	0.519	1.15	45.46	-22.26	
	[52]	0.528			-21.01	
Series 3 (fig. 10)		2.06			-307.2	
	Proposed method	0.569	2.65	63.91	-29.37	0.044
Series 4 (fig. 11)	[24]	0.643			-52.72	
	Proposed method	0.514	7.85	56.7	32.48	0.038
Series 2 (fig. 12)	[24]	0.543			-22.80	
	Proposed method	0.559	3.14	65.3	-26.63	0.037
Series 1 (fig. 13)	[24]	0.555			-15.78	
	Proposed method	0.642	13.58	121.9	106.1	0.040

Table 4: Noise parameter estimation for a Sensicam QE camera.

The exposure time being equal to 13 ms, the flickering illumination is integrated and gives a quite low σ_{γ} . Consequently the accuracy of the estimation of μ , hence σ , is moderate (see Remark 2 in Section 3.2). Additionally, a quite strong dark signal non-uniformity due to the cooling device is noticed in [33] (which also measures the offset to $\mu = 49$); this may explain a part of the variability of the measurements. Since the acquisition frequency is constant, light flickering yields a periodic σ_{γ} due to the neon light powered by the 50 Hz AC power. The sampling rate being $1/(13 \text{ ms}) = 76.9 \text{ Hz}$, therefore below the Nyquist frequency, folding gives an observed 26.9 Hz sinusoid, hence a 37.2 ms periodic pattern. This is consistent with the period estimated from Figures 10 to 13 (for instance, 7 extrema are observed in a 20 observation range, hence a period equal to $20/7 \times 13 = 37.1 \text{ ms}$). Since all series are acquired in the same room and under the same light, the same value for σ_{γ} is retrieved.

The series of Figure 10 is an example of a cluttered scene which makes the algorithm by Foi et al. to fail. This figure shows a front view of a composite specimen. Elongated chips are pieces of sunflower stem bark and light aggregates pieces of pith [50]. Since the acquisition frequency is constant, light flickering yields a periodic σ_{γ} due to the neon light powered by the 50Hz AC power. We can see that the $v_*(t)$ against $v^*(t)$ plot is quite scattered. Before flickering compensation, the variance against intensity expectation plot shows a quadratic trend, as predicted by (23-24). It changes to the linear relation with the corrected variance shown in (48). Points whose variance

can mainly be explained by vibrations (green points) are of course not adequately corrected, hence move away from the linear trend.

The series of Figure 11 depicts an easy-to-segment scene, for which the method of [24] works better than in the preceding case, but still does not give an accurate estimation. While the proposed method is able to estimate the slope of the linear trend quite accurately, the intercept estimation is inaccurate, hence a poor σ estimation.

The series of Figure 12 highlights an interesting phenomenon to which the proposed method is sensitive. An explanation for the graph of the variance of \hat{u} against the expectation of u seems to be that, in this scene, a small area is illuminated by a different neon light than the rest of the scene. The two lights have the same fluctuation amplitude (hence it cannot be noticed on the plot of the variance against the expected intensity), but they apparently show out-of-phase fluctuations (hence the pixels from the small area are not adequately corrected, giving the blue points out of the main linear trend). Here, there are a few such pixels, hence they do not prevent to reliably estimate the slope and intercept with linear regression. It seems to us that the same phenomenon occurs in the series of Figure 13 but here the slope and intercept are strongly affected by these pixels, giving inaccurate estimations.

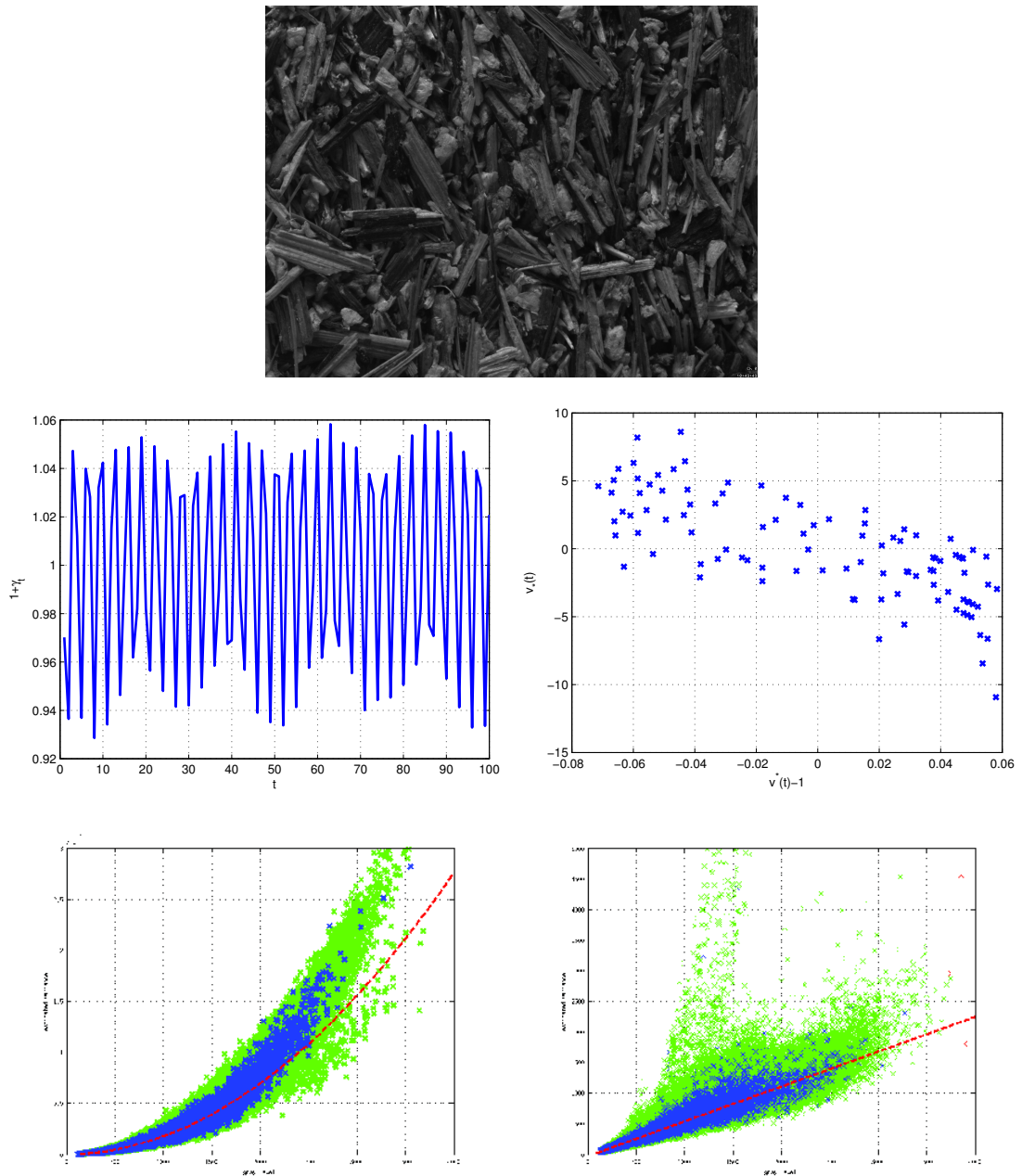


Figure 10: Sensicam QE. From top to bottom and left to right: an image from the series; estimation of the relative fluctuation of the light $1 + \gamma_t$; graph of $v_*(t)$ against $v^*(t) - 1$; graph of the sample variance of $u(x, y, t)$ against the sample mean of $u(x, y, t)$; graph of the sample variance of $\hat{u}(x, y, t)$ against the sample mean of $u(x, y, t)$.

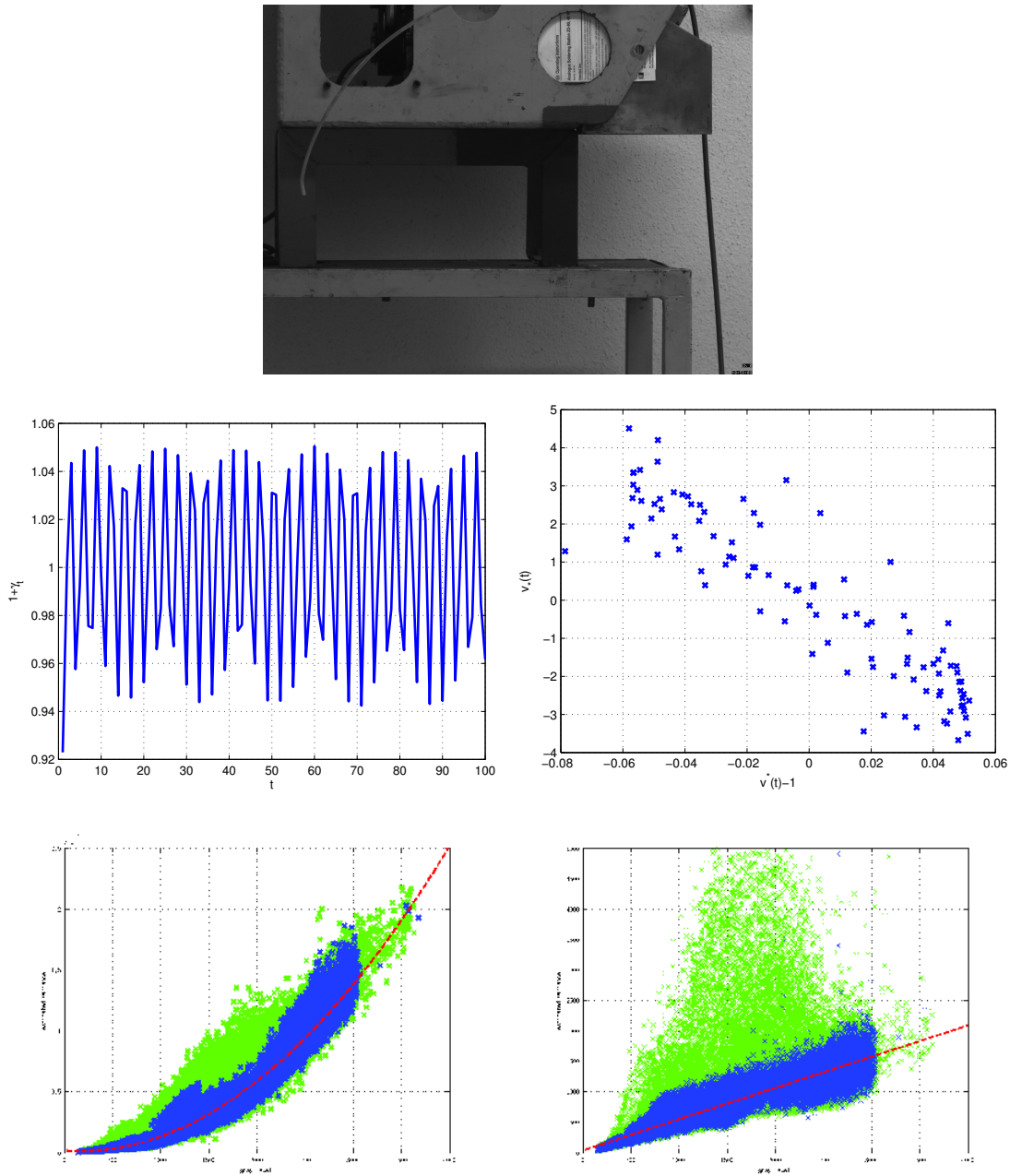


Figure 11: Sensicam QE. From top to bottom and left to right: an image from the series; estimation of the relative fluctuation of the light $1 + \gamma_t$; graph of $v_*(t)$ against $v^*(t) - 1$; graph of the sample variance of $u(x, y, t)$ against the sample mean of $u(x, y, t)$; graph of the sample variance of $\hat{u}(x, y, t)$ against the sample mean of $u(x, y, t)$.

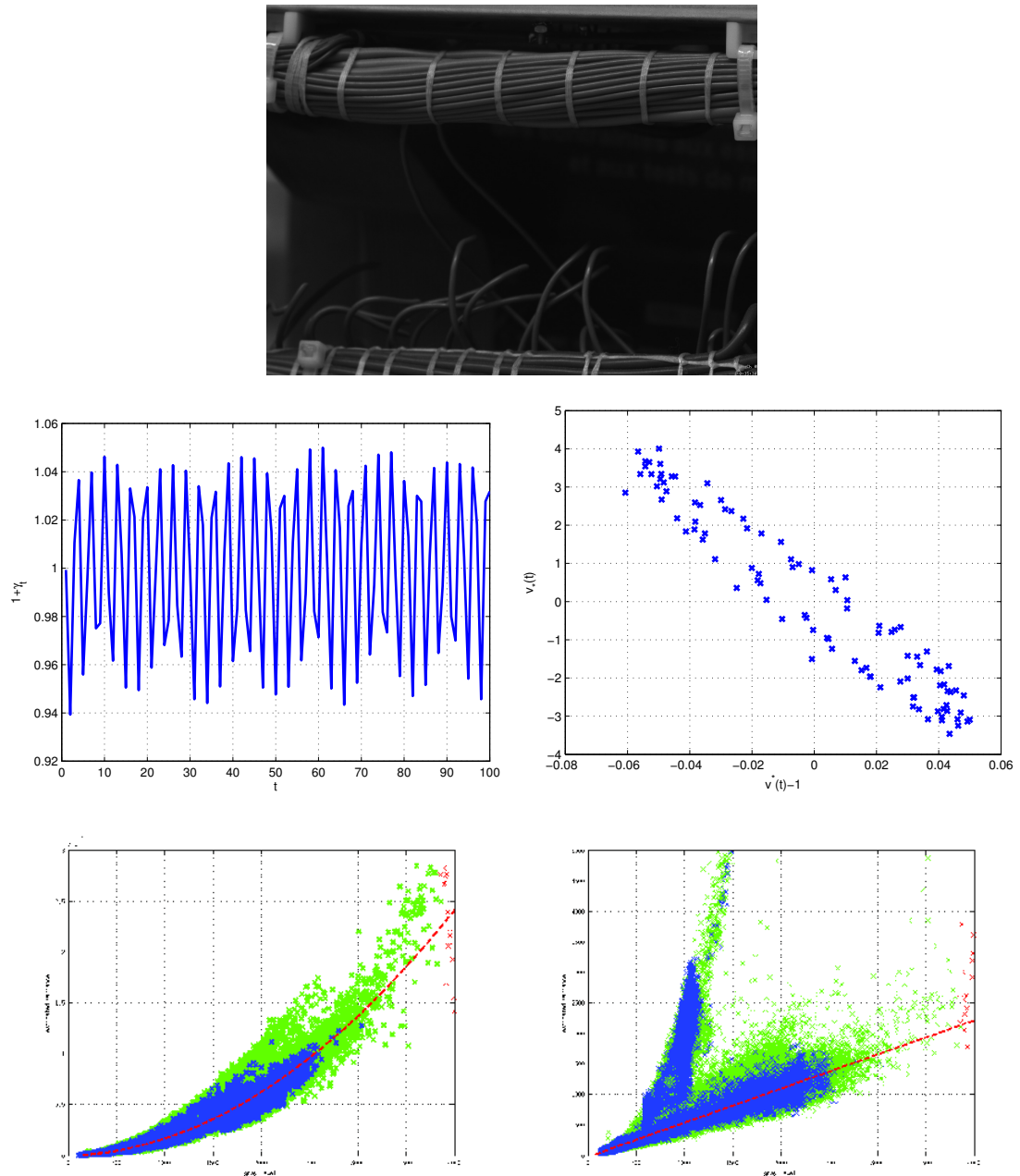


Figure 12: Sensicam QE. From top to bottom and left to right: an image from the series; estimation of the relative fluctuation of the light $1 + \gamma_t$; graph of $v_*(t)$ against $v^*(t) - 1$; graph of the sample variance of $u(x, y, t)$ against the sample mean of $u(x, y, t)$; graph of the sample variance of $\hat{u}(x, y, t)$ against the sample mean of $u(x, y, t)$.

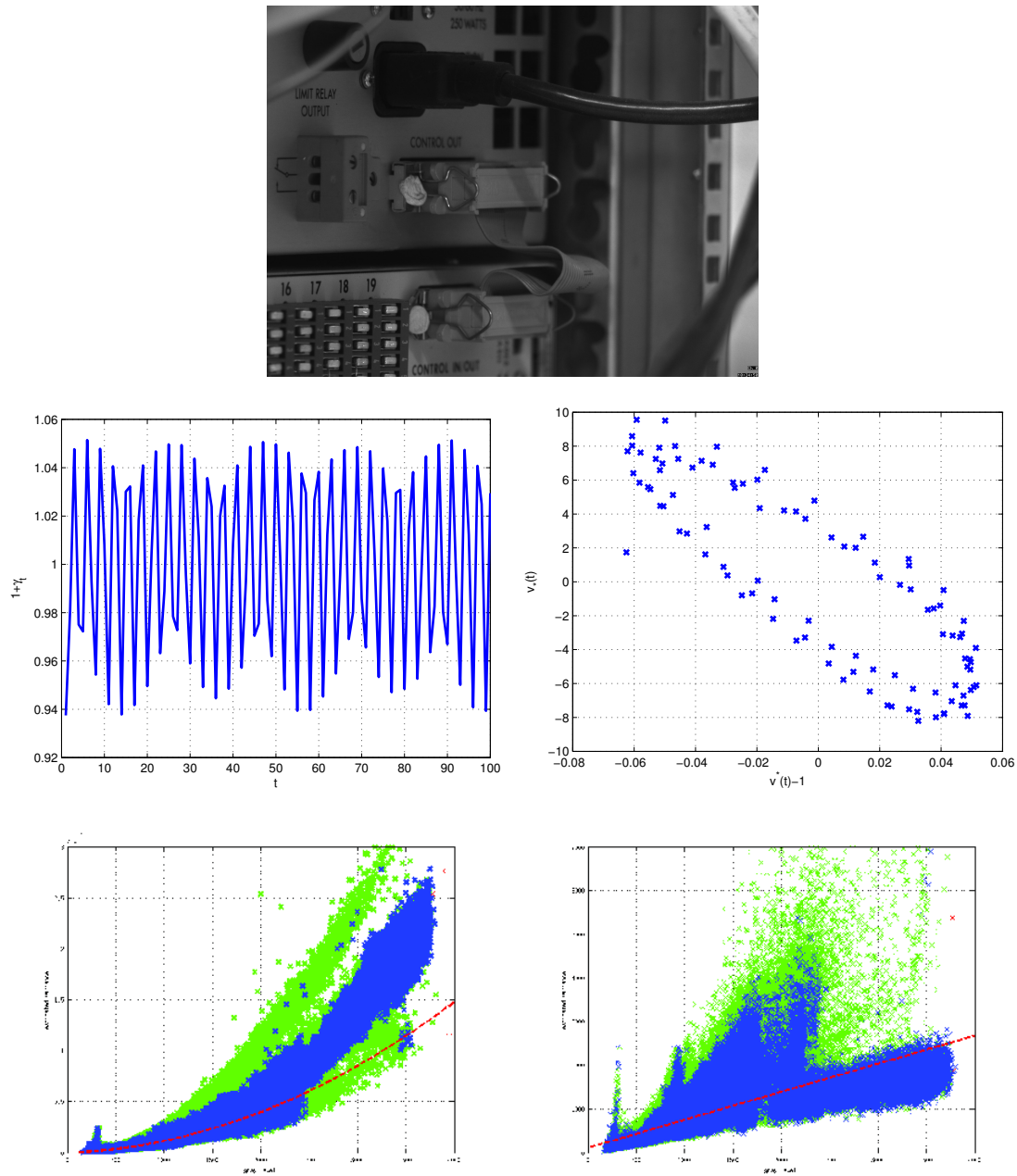


Figure 13: Sensicam QE. From top to bottom and left to right: an image from the series; estimation of the relative fluctuation of the light $1 + \gamma_t$; graph of $v_*(t)$ against $v^*(t) - 1$; graph of the sample variance of $u(x, y, t)$ against the sample mean of $u(x, y, t)$; graph of the sample variance of $\hat{u}(x, y, t)$ against the sample mean of $u(x, y, t)$.

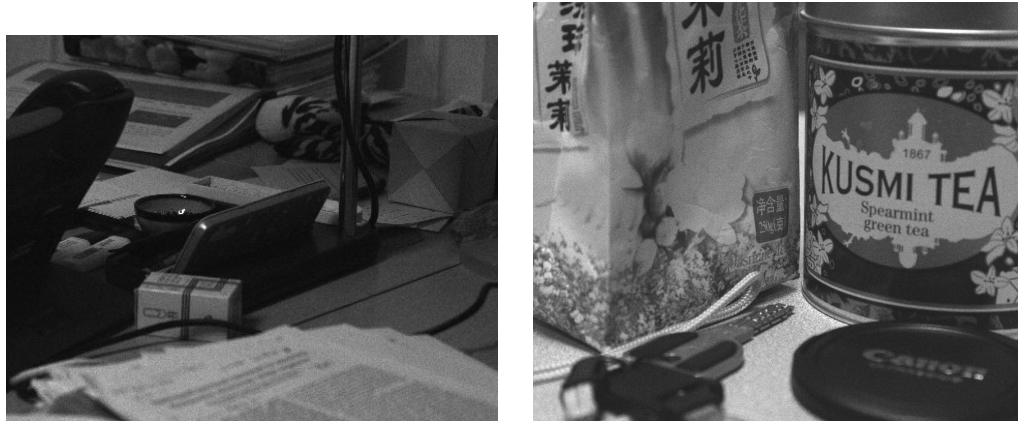


Figure 14: Left: cluttered scene for the Canon EOS 350D experiment; Right: cluttered scene for the Canon EOS 6D experiment.

4.3.2 Canon EOS 350D and EOS 6D cameras

Two Canon DSLR cameras (the 12-bit EOS 350D with an APS-C sensor and the 14-bit EOS 6D with a full-frame sensor) shoot two different scenes illuminated by a neon light: an X-Rite Colorchecker and a cluttered scene (textured objects lying on a desk) as illustrated in Figure 14. Several ISO values are tested and the corresponding exposure time t (depending on the aperture³) are given. A series of 100 raw images is linearly processed with `dcraw`⁴ and the four Bayer color channels are extracted, namely R, G1, G2, B. For the record, the EOS350D series were imaged with a 50mm focal length, and the EOS6D series with a 58mm focal length. In Tables 5 to 8, we give:

1. the values obtained by the photon transfer method⁵ (μ estimated independently over a short exposure dark frame image);
2. the output of the software by Foi et al. based on a single image (hence not affected by flickering) which estimates g and $\sigma^2 - g\mu$;
3. the results of the proposed method;
4. the estimation of the slope g and the intercept $\sigma^2 - g\mu$ of a regression line from $(E(u), \text{Var}(u))$, disregarding the quadratic trend.

ISO settings marked with an asterisk are processed with the method of Section 3.5 to deal with the rolling shutter effect.

Some results by the method [24] suggest that the default software parameters might not be adequate in some situations. The over-estimation of g by the fourth method (which does not

³The f-numbers are f/2.8 (ISO 100 and 200) and f/4.0 (ISO 400 to 1600) for the EOS350D / Colorchecker experiment, f/3.5 for the EOS350D / Clutter experiment, f/4 for the EOS6D / Colorchecker experiment, and f/6.3 for the EOS6D / Clutter experiment.

⁴available at <http://www.cybercom.net/~dcoffin/dcraw/>
Options: `dcraw -c -D -4 -r 1 1 1 1`

⁵EOS 350D: from www.astrosurf.com/comolli/strum41.htm
EOS 6D: from www.astrosurf.com/comolli/strum54.htm

take the quadratic trend into account) shows that it is important to correct flickering, especially for high ISO values hence fast shutter speeds. We can see that the proposed method not only correctly estimates g , but also μ and most of the time also σ .

Concerning the exposure time, since the neon light is powered by 50 Hz current, its flickering should not be noticeable for low ISO values because of photon integration over an exposure time lower than several tenths of second. However, σ_γ is estimated at less than 1% for $t \simeq 1/10s$, and $\sigma_\gamma \simeq 15\%$ for $t \simeq 1/200s$, see Table 9. This confirms that, here, the light flickering has a noticeable effect mainly for high ISO. In addition, it shows that a slight variability of the actual exposure, possibly due to mechanical or electronic imperfections, can be measured. It should be noted that, as we can expect, similar exposure times give similar flickering intensity. Except for some situations, the flickering intensity seems to be smaller in the green channels than in the red and blue channels. This may be explained by the sensitivity of these channels to the neon light spectrum. Furthermore, the small values of σ_γ explain the poorer estimation of μ for low ISO, hence of σ (σ^2 is estimated to a negative value in some cases, a “-” sign emphasizes it in Tables 6 and 7). Moreover, the increasing σ_γ makes the bias in the linear method to increase with ISO.

The results in Table 9 also show that the proposed estimation of the vibration parameters is quite reliable, since they are within the same order of magnitude for the four channels from the same series. Comparing with Table 5, we can see that the effect of the vibrations tends to vanish when the exposure time increases because of the longer integration time.

Figures 15 to 17 illustrate the results obtained with the Canon EOS6D camera with the cluttered scene. The higher the ISO, the faster the shutter speed, and the larger σ_γ . Consequently, the estimation of μ is improved for the largest ISO values, which can be seen on the graph of $v^*(t)$ against $v_*(t)$ which gets closer to a straight line. The quadratic trend is also all the more pronounced as σ_γ increases, as predicted by (23). The departure of the green points (corresponding to edge pixels) from the trend is stronger in the case of low σ_γ (low ISO). This corresponds to the fact that, in this case, the quadratic term overwhelms the bias term associated to the image gradient. It can be seen on Figure 17 that $\gamma_t(y)$ actually varies when a fast shutter speed is used. When the rolling shutter effect is not taken into account, the quadratic trend is not corrected, in contrast to the use of the localized $\gamma_t(y)$.

ISO	t (sec.)	1. Photon transfer method				2. Foi et al.				3. Proposed method				4. Linear estimation					
		g	σ	μ	$\sigma^2 - g\mu$	g	$\sigma^2 - g\mu$	g	σ	μ	$\sigma^2 - g\mu$	g	σ	μ	$\sigma^2 - g\mu$	g	σ	μ	$\sigma^2 - g\mu$
EOS 350D Colorch.	100	1/15	0.096	2.21	-19.92	0.111	-24.80	0.091	2.11	259.9	-19.15	0.120	-28.49						
	200	1/30	0.191	2.38	-44.57	0.201	-47.77	0.180	2.16	255.9	-41.45	0.208	-50.61						
	400	1/30	0.384	2.88	-91.92	0.391	-94.03	0.366	2.62	259.6	-88.24	0.431	-109.8						
	800 *	1/60	0.762	4.07	-182.1	0.774	-183.8	0.733	2.84	252.2	-176.7	1.800	-532.5						
	1600 *	1/125	1.531	6.36	-355.3	1.548	-358.2	1.488	5.318	258.4	-356.1	3.386	-1004.1						
EOS 6D Colorch.	100	1/3	0.176	4.85	-338.6	0.976	-2879.5	0.212	3.85	2112.4	-432.1	0.274	-596.1						
	200	1/8	0.361	4.93	-735.6	0.948	-2510.7	0.382	-	2067.5	-795.9	0.449	-962.9						
	400	1/15	0.705	5.31	-1442	0.954	-2040.3	0.729	-	2051.2	-1514.1	0.886	-1907.3						
	800 *	1/40	1.372	6.10	-2053.4	1.804	-4122	1.324	4.034	2058.7	-2708.5	1.541	-3257.5						
	1600 *	1/80	2.69	7.91	-5534	3.057	-6340.0	2.627	5.60	2049.9	-5354.2	6.45	-14543.1						
EOS 350D Clutter	100	1/13	0.096	2.21	-19.92	0.151	-36.15	0.101	1.70	238.7	-21.12	0.158	-37.84						
	200	1/30	0.191	2.38	-44.57	0.242	-57.90	0.189	2.12	253.1	-43.29	0.214	-50.90						
	400	1/60	0.384	2.88	-91.92	0.417	-99.2	0.385	3.88	262.7	-86.1	0.694	-180.0						
	800 *	1/125	0.762	4.07	-182.1	0.822	-197.4	0.735	4.39	262.1	-173.5	1.248	-323.1						
	1600 *	1/250	1.531	6.36	-355.3	1.622	-377.7	1.539	7.88	261.2	-340.0	3.88	-1022.4						
EOS 6D Clutter	100	1/2	0.176	4.85	-338.6	0.321	-685.31	0.197	5.96	2179.2	-393.6	0.197	-391.9						
	200	1/5	0.361	4.93	-735.6	0.442	-920.0	0.368	7.522	2196.9	-751.89	0.342	-695.8						
	400	1/10	0.705	5.31	-1442	0.814	-1693.4	0.720	9.05	2169.8	-1479.4	0.683	-1391.5						
	800	1/20	1.372	6.10	-2053.4	1.494	-3088.6	1.296	3.31	2041.4	-2634.0	1.313	-2675.3						
	1600 *	1/40	2.69	7.91	-5534	2.81	-5722.1	2.54	12.03	2083.0	-5143.8	5.66	-12990						
EOS 6D Clutter	3200 *	1/80	5.12	11.77	-10355	5.36	-10862	4.99	17.28	2076.9	-10071	10.88	-24941						
	6400 *	1/160	10.52	19.03	-21131	10.86	-21900	10.33	27.47	2084.3	-20766	56.36	-141180						

Table 6: Estimating camera parameters with Green 1 channel.

ISO	1. Photon transfer method				2. Foi et al.				3. Proposed method				4. Linear estimation			
	t (sec.)	g	σ	μ	$\sigma^2 - g\mu$	g	$\sigma^2 - g\mu$	g	σ	μ	$\sigma^2 - g\mu$	g	σ	μ	$\sigma^2 - g\mu$	
EOS 350D Colorch.	100	1/15	0.096	2.21	256	-19.92	0.108	-24.60	0.093	2.00	260.0	0.122	2.00	260.0	-20.09	
	200	1/30	0.191	2.38	256	-44.57	0.197	-46.26	0.182	2.15	260.0	0.215	2.15	260.0	-42.65	
	400	1/30	0.384	2.88	256	-91.92	0.396	-94.09	0.392	2.39	255.2	0.540	2.39	255.2	-94.41	
	800 *	1/60	0.762	4.07	256	-182.1	0.760	-180.5	0.729	3.51	256.8	1.589	3.51	256.8	-174.7	
	1600 *	1/125	1.531	6.36	256	-355.3	1.573	-369.4	1.539	5.45	255.1	3.105	5.45	255.1	-362.8	
EOS 6D Colorch.	100	1/3	0.176	4.85	2047	-338.6	1.194	-4033.0	0.215	2.11	2072.3	0.265	2.11	2072.3	-441.3	
	200	1/8	0.361	4.93	2047	-735.6	0.988	-2603.6	0.986	2.83	2105.1	0.441	2.83	2105.1	-804.0	
	400	1/15	0.705	5.31	2047	-1442	1.023	-2342.2	0.732	-	2073.3	0.732	-	2073.3	-1523.7	
	800 *	1/40	1.372	6.10	2047	-2053.4	1.630	-3486.5	1.314	3.58	2057.5	1.402	3.58	2057.5	-2690.8	
	1600 *	1/80	2.69	7.91	2047	-5534	3.146	-6577.9	2.62	5.46	2050.3	6.23	5.46	2050.3	-5339.7	
	3200 *	1/160	5.12	11.77	2047	-10355	5.699	-11687	5.15	9.46	2045.3	25.77	9.46	2045.3	-10442	
	6400 *	1/320	10.52	19.03	2047	-21131	11.01	-22171	10.51	16.04	2043.3	81.40	16.04	2043.3	-21227	
EOS 350D Clutter	100	1/13	0.096	2.21	256	-19.92	0.139	-31.79	0.106	1.724	242.5	0.161	1.724	242.5	-22.74	
	200	1/30	0.191	2.38	256	-44.57	0.237	-56.00	0.189	2.16	253.8	0.205	2.16	253.8	-43.31	
	400	1/60	0.384	2.88	256	-91.92	0.421	-100.24	0.384	3.86	261.3	0.715	3.86	261.3	-85.42	
	800 *	1/125	0.762	4.07	256	-182.1	0.809	-193.0	0.737	4.16	259.5	1.212	4.16	259.5	-173.8	
	1600 *	1/250	1.531	6.36	256	-355.3	1.621	-380.2	1.530	7.73	260.7	3.79	7.73	260.7	-339.1	
EOS 6D Clutter	100	1/2	0.176	4.85	2047	-338.6	0.270	-559.7	0.206	5.74	2177.9	0.190	5.74	2177.9	-416.6	
	200	1/5	0.361	4.93	2047	-735.6	0.431	-893.0	0.357	6.95	2169.6	0.336	6.95	2169.6	-727.0	
	400	1/10	0.705	5.31	2047	-1442	0.821	-1707.7	0.698	11.16	2224.1	0.664	11.16	2224.1	-1428.7	
	800	1/20	1.372	6.10	2047	-2053.4	1.493	-3088.3	1.302	8.68	2092.6	1.287	8.68	2092.6	-2648.9	
	1600 *	1/40	2.69	7.91	2047	-5534	2.799	-5739.7	2.546	12.63	2090.6	4.50	12.63	2090.6	-5162.7	
	3200 *	1/80	5.12	11.77	2047	-10355	5.411	-11018	4.989	16.45	2071.8	8.86	16.45	2071.8	-10066	
6400 *	1/160	10.52	19.03	2047	-21131	10.93	-21999	10.35	26.33	2080.1	34.33	26.33	2080.1	-20842		

Table 7: Estimating camera parameters with Green 2 channel.

ISO	t (sec.)	1. Photon transfer method				2. Foi et al.				3. Proposed method				4. Linear estimation	
		g	σ	μ	$\sigma^2 - g\mu$	g	$\sigma^2 - g\mu$	g	σ	μ	$\sigma^2 - g\mu$	g	$\sigma^2 - g\mu$	g	$\sigma^2 - g\mu$
EOS 350D Colorch.	100	1/15	0.096	2.21	256	-19.92	0.095	-19.87	0.091	2.02	253.6	-19.03	0.110	-24.54	
	200	1/30	0.191	2.38	256	-44.57	0.183	-41.83	0.179	2.06	252.6	-41.05	0.201	-47.54	
	400	1/30	0.384	2.88	256	-91.92	0.373	-87.87	0.350	2.68	257.8	-83.15	0.390	-95.09	
	800 *	1/60	0.762	4.07	256	-182.1	0.749	-176.7	0.714	3.11	253.7	-171.5	1.515	-399.0	
	1600 *	1/125	1.531	6.36	256	-355.3	1.513	-348.0	1.449	4.46	252.3	-345.7	2.839	-740.68	
EOS 6D Colorch.	100	1/3	0.176	4.85	2047	-338.6	0.669	-1599.5	0.197	5.678	2140.5	-390.2	0.206	-409.6	
	200	1/8	0.361	4.93	2047	-735.6	0.431	-864.3	0.341	4.68	2064.3	-682.9	0.382	-775.5	
	400	1/15	0.705	5.31	2047	-1442	0.801	-1651.7	0.674	4.76	2052.1	-1359.5	0.777	-1592.4	
	800 *	1/40	1.372	6.10	2047	-2053.4	1.433	-2936	1.270	6.49	2054.2	-2566.2	1.384	-2829.1	
	1600 *	1/80	2.69	7.91	2047	-5534	2.711	-5493	2.583	6.869	2043.7	-5230.9	6.207	-10969	
3200 *	1/160	5.12	11.77	2047	-10355	5.231	-10542	5.28	10.34	2043.7	-10673	17.91	-38050		
6400 *	1/320	10.52	19.03	2047	-21131	10.63	-21342	10.88	15.84	2039.4	-21938	55.00	-117553		
EOS 350D Clutter	100	1/13	0.096	2.21	256	-19.92	0.108	-22.73	0.093	1.90	244.0	-19.01	0.129	-29.15	
	200	1/30	0.191	2.38	256	-44.57	0.211	-49.02	0.181	2.31	257.0	-41.18	0.199	-46.55	
	400	1/60	0.384	2.88	256	-91.92	0.395	-93.80	0.371	3.44	259.7	-84.45	0.632	-159.9	
	800 *	1/125	0.762	4.07	256	-182.1	0.785	-186.9	0.715	3.88	257.7	-169.1	1.191	-302.7	
	1600 *	1/250	1.531	6.36	256	-355.3	1.64	-385.2	1.507	7.35	258.6	-335.8	3.40	-876.2	
EOS 6D Clutter	100	1/2	0.176	4.85	2047	-338.6	48.28	-157542	0.171	5.41	2096.1	-329.2	0.170	-325.8	
	200	1/5	0.361	4.93	2047	-735.6	0.427	-863.4	0.339	5.96	2098.2	-674.94	0.311	-616.4	
	400	1/10	0.705	5.31	2047	-1442	0.768	-1361	0.668	7.48	2098.4	-1345.3	0.629	-1263.7	
	800	1/20	1.372	6.10	2047	-2053.4	1.427	-2903.5	1.261	8.07	2071.7	-2546.7	1.237	-2500.0	
	1600 *	1/40	2.69	7.91	2047	-5534	2.718	-5515.8	2.49	12.73	2086	-5035.4	3.59	-7384.2	
3200 *	1/80	5.12	11.77	2047	-10355	5.356	-10844	4.950	16.76	2074.5	-9987	7.39	-15289		
6400 *	1/160	10.52	19.03	2047	-21131	10.92	-22017	10.33	22.44	2063.4	-20803	24.25	-50809		

Table 8: Estimating camera parameters with Blue channel.

ISO	channel	σ_α	σ_β	$\text{Cov}_{\alpha,\beta}$	σ_γ
100	R	0.013	0.0042	2.9e-05	0.011
	G1	0.0077	0.0022	8e-05	0.009
	G2	0.0078	0.003	-7.5e-06	0.0086
	B	0.015	0.0062	5e-06	0.012
200	R	0.0091	0.0092	0.00012	0.011
	G1	0.0075	0.0059	4.5e-05	0.0088
	G2	0.008	0.002	6e-05	0.0087
	B	0.013	0.004	0.00011	0.014
400	R	0.0081	0	8.8e-06	0.015
	G1	0.0079	0.0027	-1.2e-05	0.014
	G2	0.022	0.04	-0.00074	0.033
	B	0.0093	0.0055	5.4e-05	0.017
800	R	0.0039	0.0053	0.00015	0.060
	G1	0	0.0012	8.8e-05	0.046
	G2	0.0037	0.0035	7.4e-05	0.046
	B	0.0059	0.0088	0.00031	0.07
1600	R	0.025	0.0087	0.00062	0.076
	G1	0.014	0.0056	3.6e-05	0.058
	G2	0.043	0.022	0.00027	0.13
	B	0.027	0.013	5.9e-05	0.09

Canon EOS 350D Colorchecker

ISO	channel	σ_α	σ_β	$\text{Cov}_{\alpha,\beta}$	σ_γ
100	R	0.047	0.19	-0.0086	0.0088
	G1	0.039	0.16	-0.0065	0.0088
	G2	0.039	0.16	-0.0064	0.0086
	B	0.047	0.19	-0.0086	0.0099
200	R	0.043	0.059	-0.0016	0.012
	G1	0.039	0.057	-0.0014	0.0092
	G2	0.038	0.056	-0.0013	0.0099
	B	0.037	0.059	-0.0014	0.012
400	R	0.037	0.049	-0.0014	0.057
	G1	0.028	0.045	-0.0011	0.042
	G2	0.025	0.045	-0.00099	0.042
	B	0.031	0.044	-0.0012	0.059
800	R	0.042	0.078	-0.0015	0.058
	G1	0.03	0.073	-0.001	0.042
	G2	0.026	0.074	-0.00083	0.041
	B	0.035	0.071	-0.0011	0.056
1600	R	0.066	0.043	-0.0021	0.17
	G1	0.027	0.032	-0.00035	0.12
	G2	0.027	0.03	-0.00013	0.12
	B	0.037	0.058	-0.00032	0.17

Canon EOS 350D clutter

ISO	channel	σ_α	σ_β	$\text{Cov}_{\alpha,\beta}$	σ_γ
100	R	0.0062	0.0043	5.4e-05	0.0046
	G1	0.0067	0.003	-4.3e-07	0.0042
	G2	0.0054	0.0048	1.1e-05	0.0042
	B	0.0098	0.0051	-3.9e-05	0.0069
200	R	0.0074	0.025	0.00034	0.0073
	G1	0.0083	0.039	4.4e-05	0.0062
	G2	0.0057	0.018	9.7e-05	0.0063
	B	0.012	0.012	0.0002	0.0089
400	R	0.0094	0.0069	0.00022	0.011
	G1	0.0094	0.0053	0.00011	0.0088
	G2	0.0074	0.0056	0.00013	0.0089
	B	0.014	0.0089	5.1e-05	0.012
800	R	0.012	0.034	0.00028	0.01
	G1	0.011	0.023	2.1e-05	0.013
	G2	0.013	0.22	-0.0015	0.064
	B	0.017	0.038	-0.00029	0.14
1600	R	0.026	0.031	-9.8e-06	0.053
	G1	0.014	0.024	0.0001	0.043
	G2	0.021	0.022	7.4e-05	0.042
	B	0.029	0.029	-0.00025	0.059
3200	R	0.033	0.02	-0.00051	0.13
	G1	0.018	0.013	-6.2e-05	0.10
	G2	0.025	0.013	-0.0003	0.10
	B	0.04	0.018	-0.0012	0.15
6400	R	0.029	0.0087	-0.0012	0.24
	G1	0.016	0.0099	-9.7e-05	0.19
	G2	0.016	0.011	-0.00048	0.21
	B	0.038	0.021	-0.00069	0.28

Canon EOS6D Colorchecker

ISO	channel	σ_α	σ_β	$\text{Cov}_{\alpha,\beta}$	σ_γ
100	R	0.017	0.1	-0.00072	0.0032
	G1	0.016	0.099	-0.00077	0.0046
	G2	0.016	0.099	-0.00074	0.005
	B	0.017	0.1	-0.00093	0.0046
200	R	0.018	0.082	-0.00098	0.0068
	G1	0.023	0.046	-0.00073	0.0048
	G2	0.023	0.046	-0.00073	0.0047
	B	0.022	0.047	-0.00075	0.0071
400	R	0.026	0.066	-0.0014	0.0099
	G1	0.02	0.04	-0.00059	0.0058
	G2	0.02	0.04	-0.00059	0.005
	B	0.02	0.041	-0.00061	0.0071
800	R	0.014	0.22	-0.0015	0.0098
	G1	0.028	0.076	-0.00092	0.0038
	G2	0.029	0.075	-0.00092	0.0044
	B	0.028	0.077	-0.001	0.0048
1600	R	0.036	0.059	-0.0013	0.047
	G1	0.028	0.12	-0.0015	0.028
	G2	0.028	0.12	-0.0015	0.032
	B	0.03	0.12	-0.0018	0.042
3200	R	0.029	0.052	-0.0017	0.048
	G1	0.032	0.054	-0.0015	0.042
	G2	0.03	0.054	-0.0015	0.042
	B	0.037	0.059	-0.0017	0.057
6400	R	0.054	0.097	-0.0041	0.13
	G1	0.055	0.094	-0.0039	0.11
	G2	0.053	0.095	-0.0038	0.11
	B	0.062	0.12	-0.0044	0.15

CanonEOS6D clutter

Table 9: Estimating vibrations and illumination flickering.

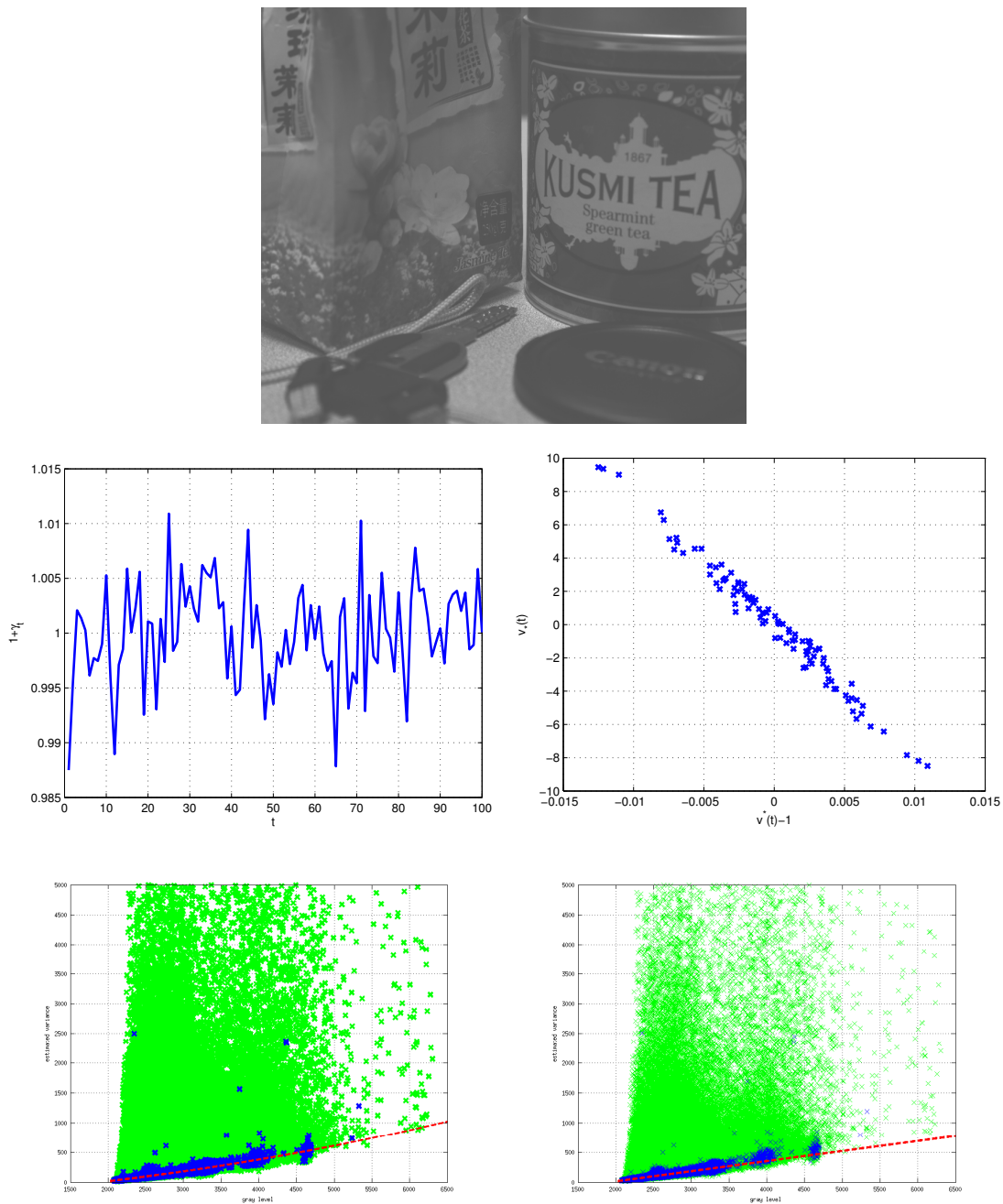


Figure 15: Canon EOS6D, cluttered scene, ISO 100. On the top: an image from the series. In the middle: estimation of the relative fluctuation of the light $1 + \gamma_t$ (image-wide estimation), and graph of $v_*(t)$ against $v^*(t) - 1$. On the bottom: graph of the sample variance of $u(x, y, t)$ against the sample mean of $u(x, y, t)$; graph of the sample variance of $\hat{u}(x, y, t)$ against the sample mean of $u(x, y, t)$.

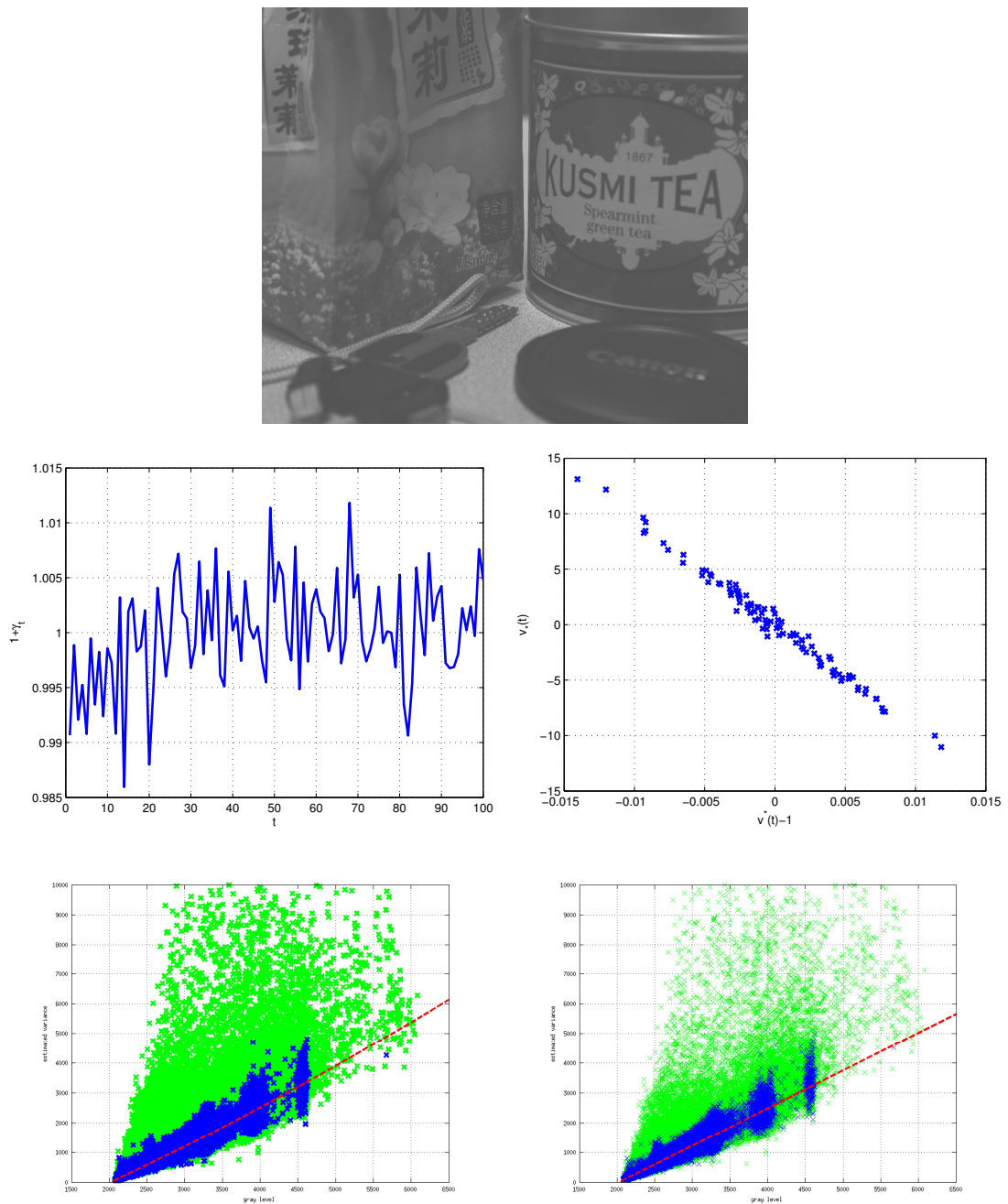


Figure 16: Canon EOS6D, cluttered scene, ISO 800. On the top: an image from the series. In the middle: estimation of the relative fluctuation of the light $1 + \gamma_t$ (image-wide estimation), and graph of $v_*(t)$ against $v^*(t) - 1$. On the bottom: graph of the sample variance of $u(x, y, t)$ against the sample mean of $u(x, y, t)$; graph of the sample variance of $\hat{u}(x, y, t)$ against the sample mean of $u(x, y, t)$.

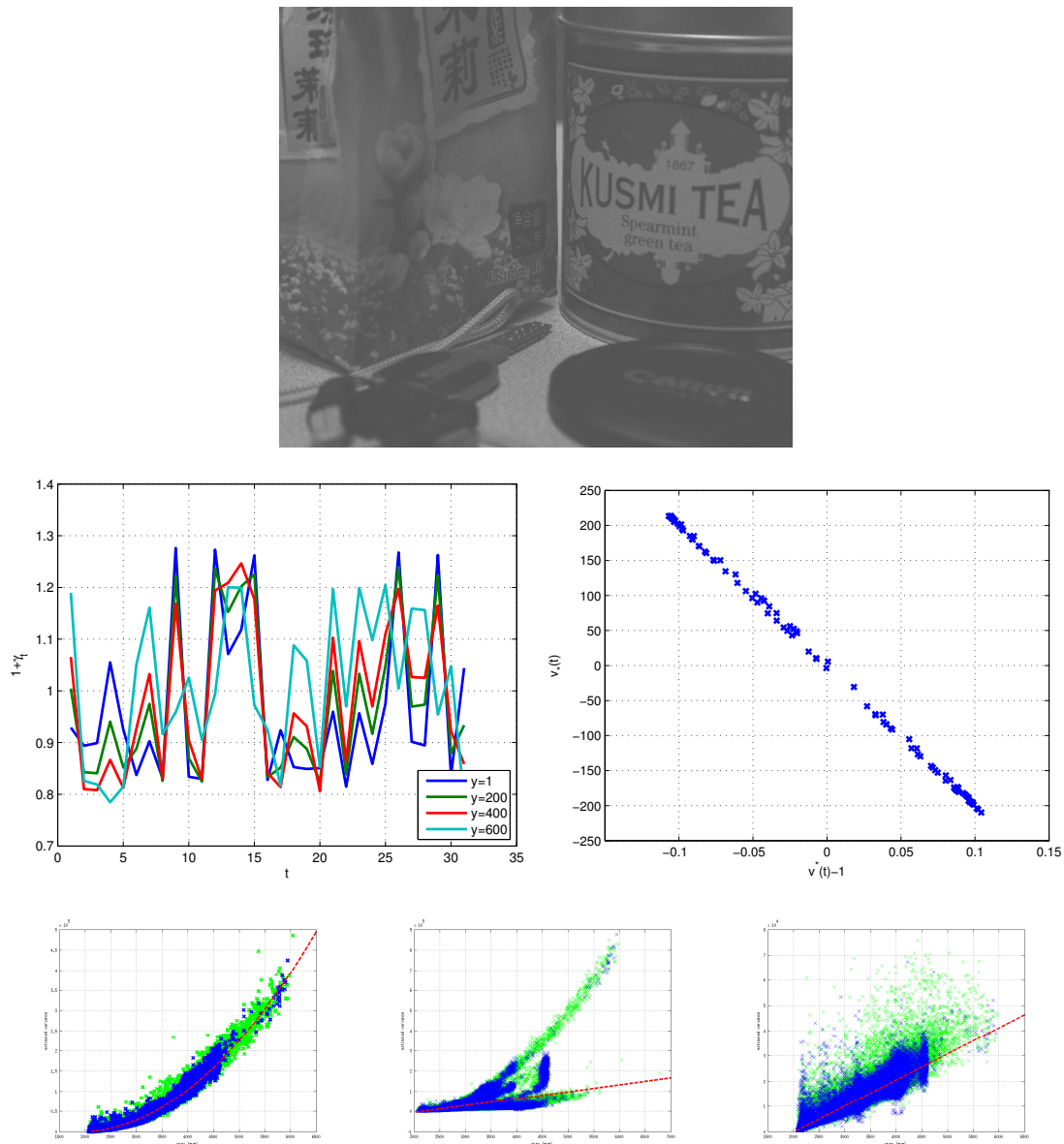


Figure 17: Canon EOS6D, cluttered scene, ISO 6400. On the top: an image from the series. In the middle: estimation of the relative fluctuation of the light $1 + \gamma_t(y)$ (for several values of y , close-up), and graph of $v_*(t)$ against $v^*(t) - 1$. On the bottom: graph of the sample variance of $u(x, y, t)$ against the sample mean of $u(x, y, t)$; graph of the sample variance of $\hat{u}(x, y, t)$ (image-wide estimation) against the sample mean of $u(x, y, t)$; graph of the sample variance of $\hat{u}(x, y, t)$ (with local estimation of $\gamma_t(y)$ to get rid of the rolling shutter effect) against the sample mean of $u(x, y, t)$.

4.3.3 Experiments with a stable light

The results of the preceding section for low ISO values, hence relative long exposure times ($t \simeq 0.5s$) compared to the neon light flickering period, show that a residual illumination flickering can still be measured, (yielding $\sigma_\gamma \simeq 0.01$, see Table 9).

The following experiments demonstrate that, even with a stable light, the variability of the shutter operation from an image of the series to the other gives a flickering illumination of the sensor, which can be actually be measured by the proposed algorithm, and makes it possible to estimate g , μ , and σ .

First, we consider a series of 100 images of a poster illuminated by an incandescent light bulb, whose flicker amplitude is known to be smaller than in the case of the neon light because of the thermal inertia of the filament, though low frequency variations can be noticed, caused by non-stationarity of the domestic current [13]. The Canon EOS350D camera was used at ISO 800, exposure time $t = 1/50s$, f-number $f/3.5$ and 17mm focal length.

Figure 18 illustrates the results of the algorithm (with the image-wide estimation of γ_t). It has given $g = 0.721$, $\sigma = 3.378$, $\mu = 256.7$, and $\sigma^2 - g\mu = -173.5$ for the red channel (similar results are obtained in the three other channels), which is close to the values of Table 5. Foi et al.'s software gives $g = 1.755$ and $\sigma^2 - g\mu = -460.9$. The illumination flickering is measured at $\sigma_\gamma = 0.012$, close to the residual flickering of the preceding section. With such a low σ_γ , the quadratic trend is barely visible in the variance against intensity plot. The vibrations are measured at $\sigma_\alpha = 0.021$ and $\sigma_\beta = 0.011$.

Second, we consider a series under natural light. The Canon EOS350D camera was used at ISO 1600, exposure time $t = 1/800s$, f-number $f/2.8$ and 23mm focal length.

Figure 19 illustrates the results of the algorithm (image-wide estimation). It has given for the red channel $g = 1.454$, $\mu = 212.9$, $\sigma^2 - g\mu = -348.3$, and σ^2 was estimated to a negative value, because of the poor estimation of μ . Foi et al.'s software gives $g = 1.580$ and $\sigma^2 - g\mu = -372.0$. The illumination flickering is measured at $\sigma_\gamma = 0.011$, still close to the residual flickering of the preceding section. The vibrations are measured at $\sigma_\alpha = 0.007$ and $\sigma_\beta = 0.056$.

As we can see, the γ_t plot shows an increasing trend. The series was actually taken early in the morning, and the sun was still rising during the three minute long acquisition. The random fluctuations along the trend are probably due to the shutter mechanism variability. The estimation of μ is not very accurate, which is explained by the large scattering of the $v_*(t)$ against $v^*(t)$ plot.

Third, we consider a series under direct sun light. The Canon EOS350D camera was used at ISO 400, exposure time $t = 1/1000s$, f-number $f/7.1$ and 50mm focal length.

Figure 20 illustrates the results of the algorithm (image-wide estimation). It has given for the red channel $g = 0.401$, $\mu = 257.0$, $\sigma^2 - g\mu = -93.2$, and $\sigma^2 = 3.14$, close to the results of Table 5. Foi et al.'s software gives $g = 0.163$ and $\sigma^2 - g\mu = 1308$ with this cluttered scene. The illumination flickering is measured at $\sigma_\gamma = 0.013$. The vibrations are measured at $\sigma_\alpha = 0.009$ and $\sigma_\beta = 0.008$.

No clear trend can be seen from the plot of γ_t , the sun being high enough in the sky at the time of the acquisition. The estimation of μ is here accurate, the $v_*(t)$ against $v^*(t)$ scatter plot being concentrated along a linear trend. This cluttered scene gives a large number of points affected by the vibrations (the green points in the sample variance plots), and interestingly, several blue points can be seen far from the main trend. This phenomenon is explained by the gentle swaying of the tree branches in the foreground, which gives pixels with a small gradient in the averaged image (hence kept by our pre-processing step), but with a large variance. It should be noted that the proposed model and algorithm assumed that the scene is static. In spite of this, parameter estimation is still possible here.

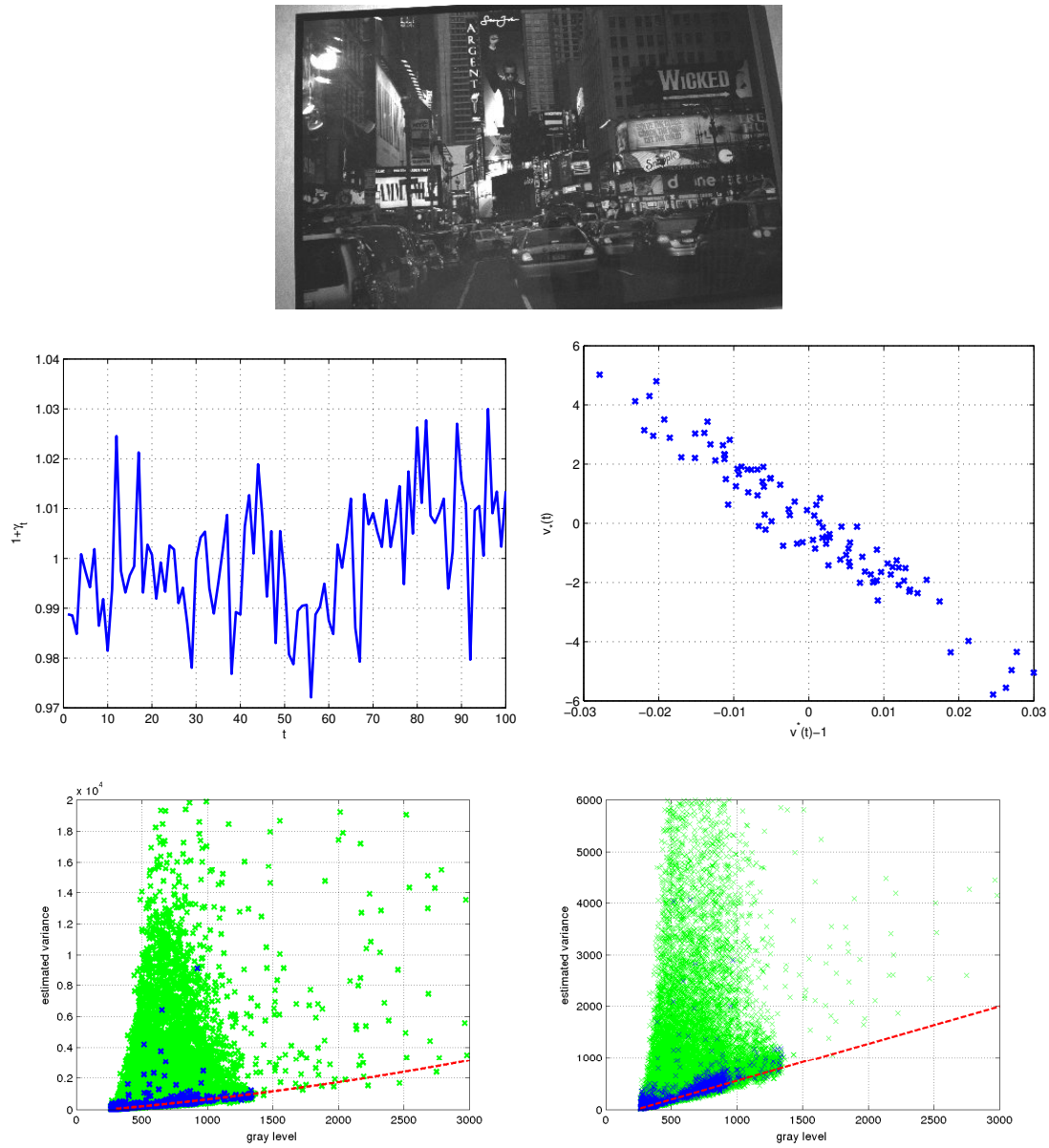


Figure 18: Canon EOS350D, poster scene, ISO 800. On the top: an image from the series. In the middle: estimation of the relative fluctuation of the light $1 + \gamma_t$ (image-wide estimation), and graph of $v_*(t)$ against $v^*(t) - 1$. On the bottom: graph of the sample variance of $u(x, y, t)$ against the sample mean of $u(x, y, t)$; graph of the sample variance of $\hat{u}(x, y, t)$ against the sample mean of $u(x, y, t)$.

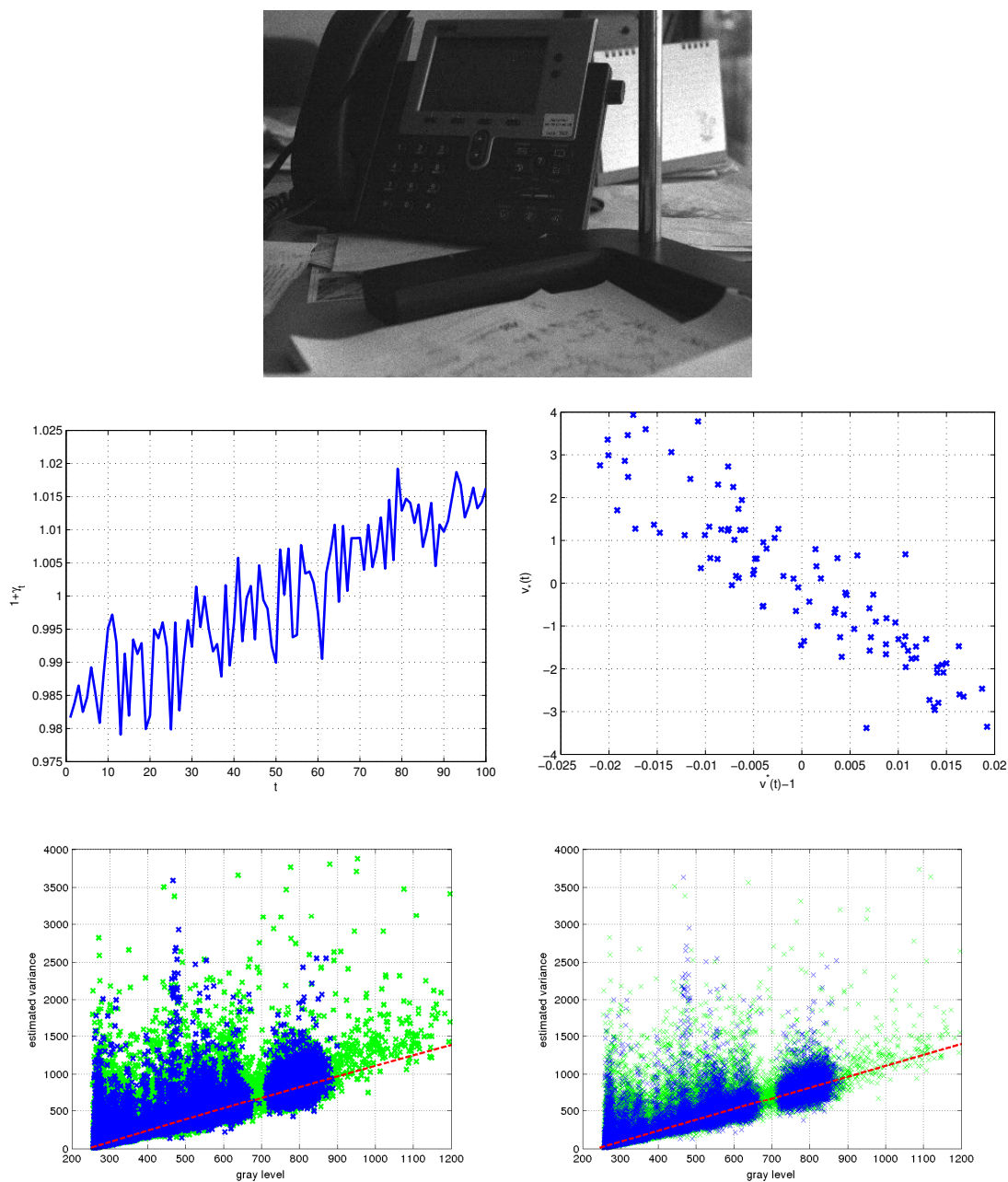


Figure 19: Canon EOS350D, shadow scene, ISO 1600. On the top: an image from the series. In the middle: estimation of the relative fluctuation of the light $1 + \gamma_t$ (image-wide estimation), and graph of $v_*(t)$ against $v^*(t) - 1$. On the bottom: graph of the sample variance of $u(x, y, t)$ against the sample mean of $u(x, y, t)$; graph of the sample variance of $\hat{u}(x, y, t)$ against the sample mean of $u(x, y, t)$.

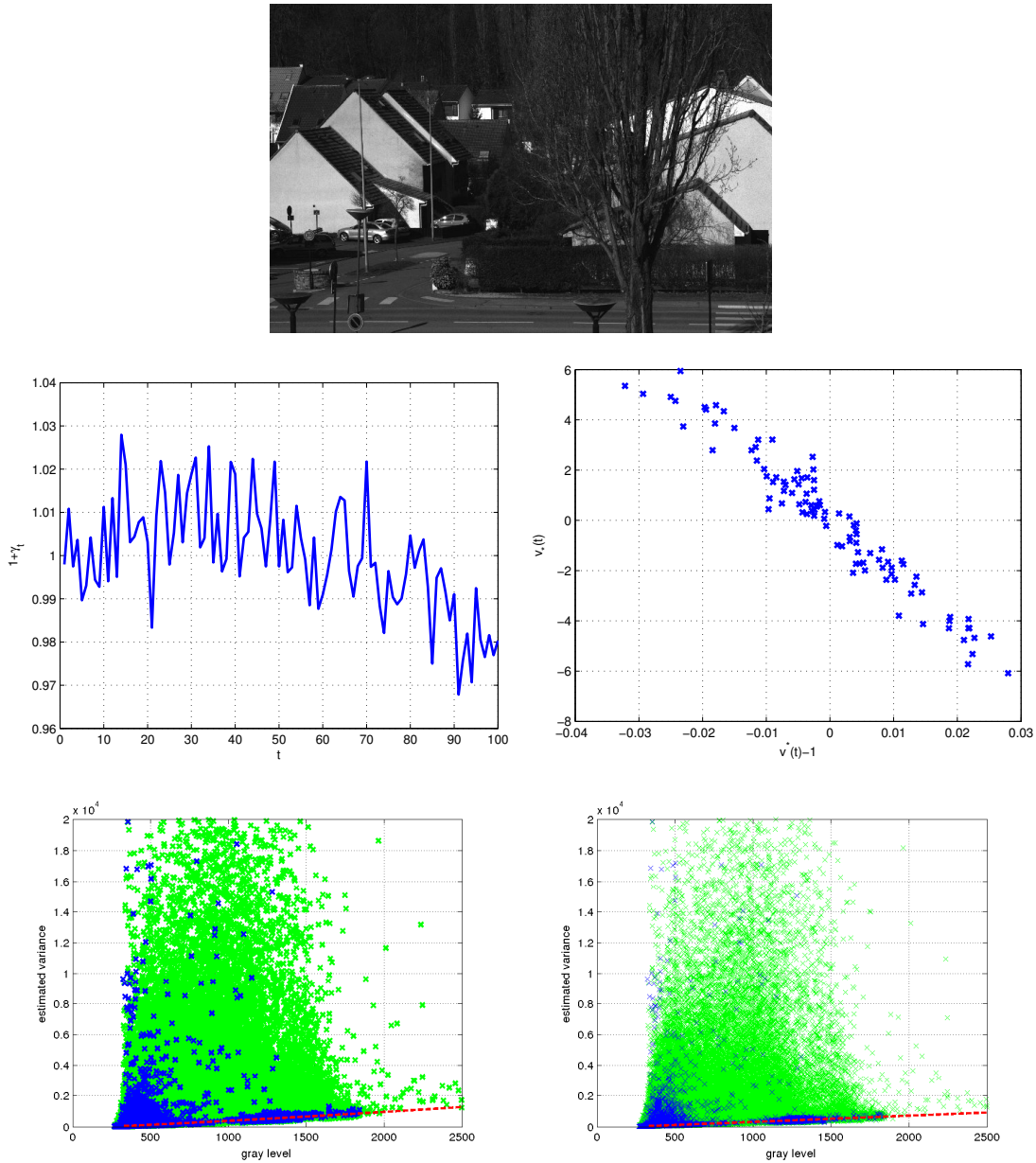


Figure 20: Canon EOS350D, outdoor scene, ISO 400. On the top: an image from the series. In the middle: estimation of the relative fluctuation of the light $1 + \gamma_t$ (image-wide estimation), and graph of $v_*(t)$ against $v^*(t) - 1$. On the bottom: graph of the sample variance of $u(x, y, t)$ against the sample mean of $u(x, y, t)$; graph of the sample variance of $\hat{u}(x, y, t)$ against the sample mean of $u(x, y, t)$.

5 Conclusion

This report discussed the effect of illumination flickering (or slightly varying exposure times) and of micro-vibrations on image noise measurements from a series of images of a static scene, within a Cox-Gaussian model. Image stacking permitted us to easily obtain sample means and sample variances without any prior segmentation step. In the presence of illumination flickering, a quadratic relation between the variance and the expected intensity was established, instead of the standard affine one. A practical algorithm was proposed, robust to the rolling shutter effect and to the vibrations. Taking benefit of the illumination flickering, it was possible to estimate the gain, the offset, and the read-out noise. A large flickering amplitude ensures a higher estimation accuracy, giving results within the range of the photon transfer method. Such an approach may be useful for multi-image denoising methods (as in [12, 37]), or for noise parameter estimation in fluorescence imaging affected by photobleaching (as in [30]), where a non-constant illumination has been noticed.

References

- [1] Sensicam QE - 1288 datasheet. Technical report, PCO Imaging, 2005.
- [2] A review of the literature on light flicker: Ergonomics, biological attributes, potential health effects, and methods in which some LED lighting may introduce flicker. Technical report, IEEE Standards P1789, 2010.
- [3] Standard 1288, standard for characterization of image sensors and cameras, release 3.0. Technical report, European Machine Vision Association (EMVA), 2010.
- [4] C. Aguerrebere, J. Delon, Y. Gousseau, and P. Musé. Study of the digital camera acquisition process and statistical modeling of the sensor raw data. Technical report, HAL, 2013.
- [5] F.J. Anscombe. The transformation of Poisson binomial and negative-binomial data. *Biometrika*, 35(3-4):246–254, 1948.
- [6] L. Azzari and A. Foi. Gaussian-Cauchy mixture modeling for robust signal-dependent noise estimation. In *Proceedings of the International Conference on Acoustics, Speech and Signal Processing (ICASSP)*, pages 5357–5361, Florence, Italy, 2014.
- [7] L. Azzari and A. Foi. Indirect estimation of signal-dependent noise with nonadaptive heterogeneous samples. *IEEE Transactions on Image Processing*, 23(8):3459–3467, 2014.
- [8] C. Badulescu, M. Grédiac, and J.-D. Mathias. Investigation of the grid method for accurate in-plane strain measurement. *Measurement Science and Technology*, 20(9):095102, 2009.
- [9] F.R. Boddekke. *Quantitative fluorescence microscopy*. PhD thesis, Technische Universiteit Delft, 1999.
- [10] J. Boulanger, C. Kervrann, P. Bouthemy, P. Elbau, J.-B. Sibarita, and J. Salamero. Patch-based nonlocal functional for denoising fluorescence microscopy image sequences. *IEEE Transaction on Medical Imaging*, 29(2):442–454, 2010.
- [11] A. Buades, B. Coll, and J.-M. Morel. A review of image denoising algorithms, with a new one. *SIAM Journal on Multiscale Modeling and Simulation*, 4(2):490–530, 2005.

-
- [12] T. Buades, Y. Lou, J.-M. Morel, and Z. Tang. A note on multi-image denoising. In *Proceeding of the International Workshop on Local and Non-Local Approximation in Image Processing*, Tuusula, Finland, 2009.
- [13] R. Cai, J.F.G. Cobben, J.M.A. Myrzik, J.H. Blom, and W.L. Kling. Flicker responses of different lamp types. *IET Generation, Transmission & Distribution*, 3(9):816–824, 2009.
- [14] M. Colom, A. Buades, and J.-M. Morel. Nonparametric noise estimation method for raw images. *Journal of the Optical Society of America A*, 31(4):863–871, 2014.
- [15] D.R. Cox. Some statistical methods connected with series of events. *Journal of the Royal Statistical Society. Series B (Methodological)*, 17(2):129–164, 1955.
- [16] D.J. Daley and D. Vere-Jones. *An introduction to the theory of point processes*, volume 1. Springer, 2nd edition, 2003.
- [17] J. Delon. Midway image equalization. *Journal of Mathematical Imaging and Vision*, 21(2):119–134, 2004.
- [18] J. Delon and A. Desolneux. Stabilization of flicker-like effects in image sequences through local contrast correction. *SIAM Journal on Imaging Sciences*, 3(4):703–734, 2010.
- [19] S. Delpretti, F. Luisier, S. Ramani, T. Blu, and M. Unser. Multiframe sure-let denoising of timelapse fluorescence microscopy images. In *Proceedings of the IEEE International Symposium on Biomedical Imaging (ISBI)*, pages 149–152, Paris, France, 2008.
- [20] B. Ellingwood and A. Tallin. Structural serviceability: Floor vibrations. *Journal of Structural Engineering*, 110(2):401–418, 1984.
- [21] H. Faraji and W.J. MacLean. CCD noise removal in digital images. *IEEE Transactions on Image Processing*, 15(9):2676–2685, 2006.
- [22] A. Foi. Clipped noisy images: Heteroskedastic modeling and practical denoising. *Signal Processing*, 89(12):2609 – 2629, 2009.
- [23] A. Foi, S. Alenius, V. Katvovnik, and K. Egiazarian. Noise measurement for raw-data of digital imaging sensors by automatic segmentation of non-uniform targets. *IEEE Sensors Journal*, 7(10):1456–1461, 2007.
- [24] A. Foi, M. Trimeche, V. Katkovnik, and K. Egiazarian. Practical Poissonian-Gaussian noise modeling and fitting for single-image raw-data. *IEEE Transactions on Image Processing*, 17(10):1737–1754, 2008.
- [25] M. Grédiac and F. Sur. Effect of sensor noise on the resolution and spatial resolution of displacement and strain maps estimated with the grid method. *Strain*, 50(1):1–27, 2014.
- [26] G.E. Healey and R. Kondepudy. Radiometric CCD camera calibration and noise estimation. *IEEE Transactions on Pattern Analysis and Machine Intelligence*, 16(3):267–276, 1994.
- [27] F. Hild and S. Roux. Comparison of local and global approaches to digital image correlation. *Experimental Mechanics*, 52(9):1503–1519, 2012.
- [28] H.T. Hytti. Characterization of digital image noise properties based on raw data. In *Proceedings of SPIE-IS&T Electronic Imaging, Image Quality and System Performance III*, volume 6059, San Jose (CA), USA, 2006.

- [29] L. Isserlis. On a formula for the product-moment coefficient of any order of a normal frequency distribution in any number of variables. *Biometrika*, 12(1-2):134–139, 1918.
- [30] A. Jezierska, C. Chaux, J.-C. Pesquet, H. Talbot, and G. Engler. An EM approach for time-variant Poisson-Gaussian model parameter estimation. *IEEE Transactions on Signal Processing*, 62(1):17–30, 2014.
- [31] A. Jezierska, J.-C. Pesquet, H. Talbot, and C. Chaux. Iterative Poisson-Gaussian noise parametric estimation for blind image denoising. In *Proceedings of the International Conference on Image Processing (ICIP)*, Paris, France, 2014.
- [32] X. Jin, Z. Xu, and K. Hirakawa. Noise parameter estimation for Poisson corrupted images using variance stabilization transforms. *IEEE Transactions on Image Processing*, 23(3):1329–1339, 2014.
- [33] D.S. Kepshire. Sub-surface diffuse fluorescence tomography: system development and feasibility studies. Master’s thesis, Thayer School of Engineering, Dartmouth College, Hanover, New Hampshire, 2006.
- [34] M. Lebrun, M. Colom, A. Buades, and J.-M. Morel. Secrets of image denoising cuisine. *Acta Numerica*, 21(1):475–576, 2012.
- [35] C. Liu, R. Szeliski, S.B. Kang, C.L. Zitnick, and W.T. Freeman. Automatic estimation and removal of noise from a single image. *IEEE Transactions on Pattern Analysis and Machine Intelligence*, 30(2):299–314, 2008.
- [36] X. Liu, M. Tanaka, and M. Okutomi. Practical signal-dependent noise parameter estimation from a single noisy image. *IEEE Transactions on Image Processing*, 23(10):4361–4371, 2014.
- [37] Z. Liu, L. Yuan, X. Tang, M. Uyttendaele, and J. Sun. Fast burst images denoising. *ACM Transactions on Graphics*, 33(6):232:1–232:9, 2014.
- [38] R. W. Lohman. Neon tube characteristics. *Electrical Engineering*, 52(5):304–307, 1933.
- [39] M. Makitalo and A. Foi. Optimal inversion of the generalized Anscombe transformation for Poisson-Gaussian noise. *IEEE Transactions on Image Processing*, 22(1):91–103, 2013.
- [40] M. Makitalo and A. Foi. Noise parameter mismatch in variance stabilization, with an application to Poisson-Gaussian noise estimation. *IEEE Transactions on Image Processing*, 23(12):5348–5359, 2014.
- [41] P. Milanfar. A tour of modern image filtering: New insights and methods, both practical and theoretical. *IEEE Signal Processing Magazine*, 30(1):106–128, 2013.
- [42] J. Molimard and L. Navarro. Uncertainty on fringe projection technique: A Monte-Carlo-based approach. *Optics and Lasers in Engineering*, 51(7):840–847, 2013.
- [43] F. Murthagh, J.L. Starck, and A. Bijaoui. Image restoration with noise suppression using a multiresolution support. *Astronomy and astrophysics*, 112:179–189, 1995.
- [44] G.W. Oehlert. A note on the Delta method. *The American Statistician*, 46(1):27–29, 1992.
- [45] B. Pan, Z. Lu, and H. Xie. Mean intensity gradient: an effective global parameter for quality assessment of the speckle patterns used in digital image correlation. *Optics and Lasers in Engineering*, 48:469–477, 2010.

-
- [46] S. Pyatykh and J. Hesser. Image sensor noise parameter estimation by variance stabilization and normality assessment. *IEEE Transactions on Image Processing*, 23(9):3990–3998, 2014.
- [47] S. Ramani, C. Vonesch, and M. Unser. Deconvolution of 3d fluorescence micrographs with automatic risk minimization. In *Proceedings of the IEEE International Symposium on Biomedical Imaging (ISBI)*, pages 732–735, Paris, France, 2008.
- [48] P. Roudot, C. Kervrann, J. Boulanger, and F. Waharte. Noise modeling for intensified camera in fluorescence imaging: Application to image denoising. In *Proceedings of the IEEE International Symposium on Biomedical Imaging (ISBI)*, pages 600–603, San Francisco (CA), USA, 2013.
- [49] P. Roudot, C. Kervrann, F. Waharte, and J. Boulanger. Lifetime map reconstruction in frequency-domain fluorescence lifetime imaging microscopy. In *Proceedings of the International Conference on Image Processing (ICIP)*, pages 2537–2540, Orlando (FL), USA, 2012.
- [50] S. Sun, M. Grédiac, E. Toussaint, J.-D. Mathias, and N. Mati-Baouche. Applying a full-field measurement technique to characterize the mechanical response of a sunflower-based biocomposite. *Experimental Mechanics*, 2015. To be published.
- [51] F. Sur and M. Grédiac. Sensor noise measurement in the presence of a flickering illumination. In *Proceedings of the International Conference on Image Processing (ICIP)*, Paris, France, 2014.
- [52] F. Sur and M. Grédiac. Sensor noise modeling by stacking pseudo-periodic grid images affected by vibrations. *IEEE Signal Processing Letters*, 21(4):432–436, 2014.
- [53] F. Sur and M. Grédiac. Towards deconvolution to enhance the grid method for in-plane strain measurement. *AIMS Inverse Problems and Imaging*, 8(1):259–291, 2014.
- [54] F. Sur and M. Grédiac. Measuring the noise of digital imaging sensors by stacking raw images affected by vibrations and illumination flickering. *SIAM Journal on Imaging Sciences*, 2015. To be published.
- [55] F. Sur and M. Grédiac. On noise reduction in strain maps obtained with the grid method by averaging images affected by vibrations. *Optics and Lasers in Engineering*, 66:210–222, 2015.
- [56] T.H. Thai, R. Cogranne, and F. Reintant. Camera model identification based on the heteroscedastic noise model. *IEEE Transactions on Image Processing*, 23(1):250–263, 2014.
- [57] M.L. Uss, B. Vozel, V.V. Lukin, and K. Chehdi. Image informative maps for component-wise estimating parameters of signal-dependent noise. *IS&T / SPIE Journal of Electronic Imaging*, 22(1):013019, 2013.
- [58] S.B. Vardeman and C.-S. Lee. Likelihood-based statistical estimation from quantized data. *IEEE Transactions on Instrumentation and Measurement*, 54(1):409–414, 2005.
- [59] B. Waegli. Investigations into the noise characteristics of digitized aerial images. *International Archives for Photogrammetry and Remote Sensing*, XXXII/2:341–348, 1998.
- [60] Y. Q. Wang, M. A. Sutton, H. A. Bruck, and H. W. Schreier. Statistical analysis of the effect of intensity pattern noise on the displacement measurement precision of digital image correlation using self-correlated images. *Experimental Mechanics*, 41(2):701–707, 2007.

- [61] Y. Q. Wang, M. A. Sutton, H. A. Bruck, and H. W. Schreier. Quantitative error assessment in pattern matching: effects of intensity pattern noise, interpolation, strain and image contrast on motion measurements. *Strain*, 45(2):160–178, 2009.



**RESEARCH CENTRE
NANCY – GRAND EST**

615 rue du Jardin Botanique
CS20101
54603 Villers-lès-Nancy Cedex

Publisher
Inria
Domaine de Voluceau - Rocquencourt
BP 105 - 78153 Le Chesnay Cedex
inria.fr

ISSN 0249-6399